RSC Advances

PAPER

View Article Online
View Journal | View Issue

Cite this: *RSC Adv.*, 2025, **15**, 37429

Comprehensive structural insights and electrochemical evaluation of rhamnose and salicin for green corrosion protection of carbon steel in acidic medium

Faisal Al-Odail,[a] Mahmoud A. Bedair, *[b] Mohammed A. Alkhalifah[a] and Ahmed M. Abuelela*[a]

This study presents a comprehensive electrochemical and theoretical evaluation of two naturally occurring organic compounds, Rhamnose and Salicin, as green corrosion inhibitors for carbon steel in 1 M HCl. Electrochemical techniques including Potentiodynamic Polarization (PDP), Electrochemical Impedance Spectroscopy (EIS), and Electrochemical Frequency Modulation (EFM) were employed to assess inhibition performance. At a concentration of 1.0×10^{-3} M, Salicin achieved a maximum inhibition efficiency of 96.10%, while Rhamnose reached 91.91%, as determined by PDP. EIS analysis revealed a significant increase in charge transfer resistance (R_{ct}) from 19.05 Ω cm^2 (blank) to 172.27 Ω cm^2 for Salicin and 121.65 Ω cm^2 for Rhamnose. The adsorption behavior followed the Langmuir isotherm, with calculated free energies of adsorption (ΔG°_{ads}) of −33.21 kJ mol^{-1} for Salicin and −32.59 kJ mol^{-1} for Rhamnose, indicating spontaneous mixed-mode adsorption. Density Functional Theory (DFT) calculations revealed that Salicin possesses a lower energy gap (ΔE = 6.321 eV) and higher electron transfer capability (ΔN = 0.943) compared to Rhamnose (ΔE = 8.767 eV, ΔN = 0.783), suggesting superior reactivity and adsorption potential. Adsorption locator simulations confirmed stronger binding of Salicin to Fe(110) surfaces, with an adsorption energy of −230.86 kcal mol^{-1} *versus* −83.58 kcal mol^{-1} for Rhamnose. These findings highlight the potential of Salicin as a highly efficient, eco-friendly corrosion inhibitor and demonstrate the value of integrating molecular-level insights into inhibitor design.

Received 22nd August 2025
Accepted 27th September 2025

DOI: 10.1039/d5ra06243h

rsc.li/rsc-advances

1. Introduction

Corrosion is a pervasive and costly phenomenon that affects nearly every sector reliant on metallic infrastructure. According to global estimates, corrosion-related damage incurs annual losses exceeding $2.5 trillion, representing approximately 3–4% of the global GDP. This impact spans critical industries such as oil and gas, water treatment, transportation, construction, and energy, where metal degradation compromises safety, efficiency, and longevity. Among the metals most widely used, carbon steel stands out due to its mechanical strength, affordability, and adaptability. It is extensively employed in pipelines, structural components, automotive systems, and marine applications. However, its vulnerability to acidic environments necessitates the development of effective and sustainable corrosion mitigation strategies.[1–9]

In recent years, the pursuit of green corrosion inhibitors has gained momentum, driven by the dual imperative of environmental protection and industrial performance. Conventional inhibitors often involve toxic, expensive, or environmentally hazardous compounds, prompting a shift toward eco-friendly, biodegradable, and non-toxic organic molecules. These green alternatives not only reduce environmental burden but also offer cost-effective solutions for large-scale applications. The integration of corrosion control with environmental stewardship is no longer optional, it is a strategic necessity.[10–16]

Despite the abundance of literature on the synthesis of organic inhibitors, there remains a critical gap in structure-guided material design. True innovation in inhibitor development requires a deep understanding of the molecular and electronic structure of base molecules, those that serve as precursors for more complex derivatives. By analyzing the spatial arrangement of atoms and functional groups, researchers can predict how these features influence electron distribution, adsorption behavior, and surface interaction. This foundational knowledge is essential for rational design and optimization of next-generation inhibitors.[1,17–24]

[a]*Department of Chemistry, College of Science, King Faisal University, Al-Ahsa 31982, Saudi Arabia. E-mail: aabuelela@kfu.edu.sa*

[b]*Department of Chemistry, College of Science, University of Bisha, P. O. Box 511, Bisha, 61922, Saudi Arabia. E-mail: mbedair@ub.edu.sa*

To achieve such insight, advanced theoretical tools are indispensable. Techniques such as atomic charge analysis – using Hirshfeld, Electrostatic Potential (ESP) and NBO charges, Fukui reactivity indices, Frontier Molecular Orbital (FMO) mapping, and Natural Bond Orbital (NBO) donor–acceptor interactions provide a comprehensive framework for evaluating molecular reactivity. These descriptors allow for the identification of nucleophilic and electrophilic centers, prediction of adsorption sites, and assessment of electron donation and back-donation capabilities—all of which are crucial for effective corrosion inhibition.

In this work, we present a comprehensive electrochemical and theoretical investigation of two naturally occurring molecules—Rhamnose and Salicin—as green corrosion inhibitors for carbon steel in 1 M HCl. Through detailed analysis of their electronic structure, adsorption behavior, and molecular reactivity, we aim to elucidate the mechanisms underlying their inhibition performance. The novelty of this study lies in its integrated approach, combining experimental validation with in-depth quantum chemical modeling to offer a holistic perspective on corrosion inhibition. This work not only advances the understanding of base molecular frameworks but also contributes to the rational design of environmentally friendly inhibitors.

2. Experimental

2.1 Chemicals

Rhamnose and Salicin were purchased as solid reagents from Sigma-Aldrich and were dissolved in 1 M HCl to prepare the required concentrations for all experiments. Hydrochloric acid (HCl, analytical grade) was purchased from Fisher, while acetone and ethyl alcohol (both analytical grade) were obtained from Aldrich. All chemicals were used as received without further purification.

2.2 Electrochemical measurements

Electrochemical experiments were conducted using a Gamry REF600 potentiostat, and data analysis was performed with Echem Analyst 2 software (Framework version 7.10.4). A standard three-electrode configuration was employed in a 50 mL glass cell. The working electrode consisted of a polished carbon steel coupon with an exposed surface area of 1.0 cm^2, while a platinum mesh served as the counter electrode and a saturated Ag/AgCl electrode in KCl was used as the reference. All measurements were carried out at a controlled temperature of 25 ± 1 °C in 1 M HCl solution containing varying concentrations (10^{-4} to 10^{-3} M) of Rhamnose and Salicin. Prior to each test, the working electrode was immersed in the test solution and allowed to stabilize until a steady open circuit potential (OCP) was achieved, ensuring surface equilibrium and the formation of any protective layers over a period of 3600 seconds. Electrochemical Frequency Modulation (EFM) measurements were performed using a base frequency of 0.1 Hz, with modulation frequencies of 2.0 and 5.0, and an applied amplitude of 10 mV. These measurements provided insights into non-faradaic processes and adsorption kinetics. Electrochemical Impedance Spectroscopy (EIS) was conducted at the OCP across a frequency range of 100 kHz to 0.01 Hz using a 10 mV sinusoidal perturbation. The resulting impedance spectra were fitted to appropriate equivalent circuit models to extract parameters such as charge transfer resistance (R_{ct}) and double-layer capacitance (C_{dl}). Potentiodynamic polarization (PDP) curves were recorded by sweeping the potential from −250 mV to +250 mV relative to the OCP at a scan rate of 0.5 mV s^{-1}. Corrosion current density (i_{corr}) and corrosion potential (E_{corr}) were determined *via* Tafel extrapolation of the anodic and cathodic branches.

The inhibition efficiency (η) and surface coverage (θ) of Rhamnose and Salicin were calculated from EFM, PDP, and EIS data using the following equations:

$$\eta_{P,EFM}\% = 100\left(1 - \frac{i_{corr,inh}}{i_{corr,blank}}\right) \quad (1)$$

$$\eta_z\% = 100\left(\frac{R_{ct,inh} - R_{ct,blank}}{R_{ct}}\right) \quad (2)$$

2.3 Theoretical models

All quantum chemical computations were carried out using the Gaussian 16 software suite,[25,26] with molecular structures visualized and analyzed using GaussView 6. The geometries of Rhamnose and Salicin were optimized using Density Functional Theory (DFT) at the B3LYP/6-31G(d,p) level, which offers a reliable balance between computational efficiency and accuracy.[27,28] To account for solvent effects and better simulate the corrosion environment, the Polarizable Continuum Model (PCM) was employed with water as the dielectric medium (SCRF = solvent = water). Population analyses were extracted using the keyword pop = (mk, hirshfeld, nbo), enabling the calculation of molecular electrostatic potential, Hirshfeld charges, and natural bond orbitals. The options geom = connectivity and guess = save were included to ensure consistent molecular geometry and wavefunction convergence throughout the calculations. To simulate the interaction between the inhibitor molecules and the iron surface, a computational adsorption study was performed using a slab model of the Fe(110) crystal surface. The surface was constructed by cleaving the bulk iron structure along the (110) crystallographic plane, which is known for its high atomic density and stability. The model was expanded by replicating the unit cell five times along the *a*-axis and eight times along the *b*-axis, creating a sufficiently large surface area to accommodate the inhibitor molecules and minimize edge effects. To prevent artificial interactions between periodic images, a vacuum layer of 15 Å was added perpendicular to the surface (*c*-axis). The inhibitor molecules were initially placed 8 Å above the metal surface to allow for unbiased adsorption exploration. The adsorption simulations were carried out using the Adsorption Locator module within BIOVIA Materials Studio 2024, employing the COMPASSIII forcefield, which offers reliable accuracy for both organic and metallic systems. Electrostatic interactions were treated using

the Ewald summation method, suitable for periodic boundary conditions. An energy window of 100 kcal mol^{-1} was defined to retain only the most energetically favorable adsorption configurations. This setup enabled the identification of optimal binding orientations and energies, providing insight into the molecular affinity of Salicin and Rhamnose toward the iron surface.

3. Results and discussion

3.1 Electrochemical measurements

3.1.1 Potentiodynamic polarization (PDP) analysis. The PDP curves for carbon steel in 1.0 M HCl solution without and with different concentrations of Rhamnose and Salicin are shown in Fig. 1(a) and (b), respectively. The corresponding electrochemical parameters derived from the curves are presented in Table 1. As evident from Fig. 1, addition of Rhamnose and Salicin results in a sharp reduction in the current density of both anodic and cathodic branches, revealing a strong inhibitory action on the overall corrosion reaction.[29] The cathodic curves experience greater shifts compared to the anodic curves, particularly at higher concentrations of the inhibitors, revealing that the inhibitors are predominantly inhibiting the cathodic hydrogen evolution reaction.[30] Such a behavior categorizes both Rhamnose and Salicin as mixed-type inhibitors with cathodic predominance since they slow down both anodic metal dissolution and cathodic hydrogen evolution but to a different degree.[31] Interestingly, the anodic branches of the curves deviate from ideal Tafel behavior, indicating that the metal dissolution process is affected by extraneous effects, for example, adsorption of inhibitors or formation of layers on the surface. In contrast, the cathodic branches in all the concentrations investigated exhibit excellent linearity, indicating that the hydrogen evolution reaction is still activation controlled.[32] This further indicates that the inhibitors do not change the inherent mechanism of the cathodic reduction but rather act through blocking of active sites and hence retarding the reaction kinetics.[33] The blank curve (black line) shows the highest current density, typical of aggressive corrosion in uninhibited HCl solution.[34] With an increase in inhibitor concentration, the curves are displaced to lower current densities, affirming a concentration-dependent inhibition behavior.[35] Importantly, Fig. 1b (Salicin) shows a greater change in both anodic and cathodic branches compared with Fig. 1a (Rhamnose), reflecting the greater inhibitory performance of Salicin. This can be attributed to its structural features, particularly the existence of the aromatic benzene ring and the phenolic –OH group, which promote adsorption *via* π-d orbital interaction and hydrogen bonding with the steel substrate.[36] These functionalities enhance the electron-donating ability and strengthen the interaction with active corrosion sites.[37] Conversely, Rhamnose (Fig. 1a), which lacks an aromatic structure and is a monosaccharide featuring a methyl-substituted pyranose ring, exhibits a weaker inhibitory action. The polarization curve changes that it produces are less significant, especially at lower concentrations, indicating a slower adsorption process or a weaker adsorption strength.

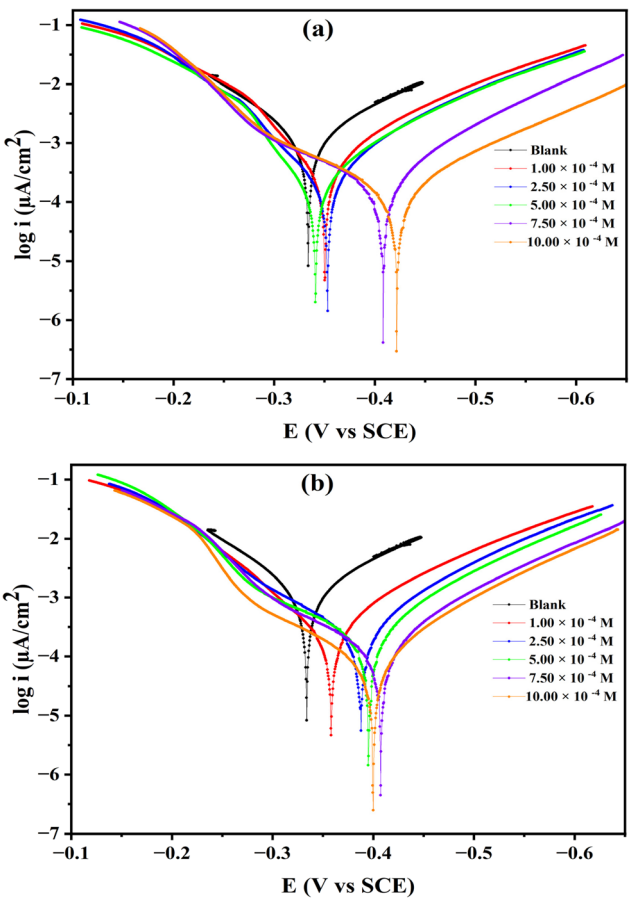

Fig. 1 Potentiodynamic polarization curves for the corrosion of carbon steel in 1.0 M HCl in absence and presence of different concentrations of Rhamnose (a) and Salicin (b) compounds at 30 °C.

As can be seen from Table 1, the presence of both inhibitors considerably moves the corrosion current density (i_{corr}) towards lower values with respect to the blank solution, showing an efficient inhibition of the corrosion process.[38] The i_{corr} decreased from 1579 μA cm^{-2} in uninhibited solution to 127.7 μA cm^{-2} and 61.57 μA cm^{-2} for the concentrations (1.0×10^{-3} M) of Rhamnose and Salicin, respectively. The corrosion potential (E_{corr}) showed small shifts towards the negative side with increasing concentration of inhibitors for both compounds, which points to a mixed-type inhibition mechanism with a pronounced cathodic effect.[39] This finding is further supported by changes in the Tafel slopes (β_a and β_c), which were influenced by the presence of the inhibitors and thus showing their effect on both anodic dissolution reactions and cathodic hydrogen evolution reactions.[40] The inhibition efficiency (η%) rose linearly with inhibitor concentration, with a maximum of 91.91% for Rhamnose and 96.10% for Salicin at 1.0×10^{-3} M. This is in agreement with the reduction of corrosion current density and rise in surface coverage (θ), suggesting effective adsorption of inhibitor molecules on the steel surface.[41] The corrosion rate (k) fell drastically with the rising concentration of the inhibitor, attesting to the protective quality of both molecules. The minimum values of corrosion rates

Table 1 Electrochemical parameters[a] for carbon steel dissolution in 1.0 M HCl solution containing different concentrations of the (Rhamnose and Salicin) inhibitors obtained from polarization measurements at 30 °C

Inhibitor name	Conc. (M)	E_{corr} *vs.* SCE (mV)	i_{corr} (μA cm^{-2})	β_a (mV dec^{-1})	$-\beta_c$ (mV dec^{-1})	k (mpy)	θ	η_p%
Blank	—	−333.7	1579	104.1	136.4	721.50	—	—
Rhamnose	1.00×10^{-4}	−350.2	749.7	103.2	139.7	342.60	0.5252	52.52
	2.50×10^{-4}	−353.0	419.6	92.07	123.3	191.80	0.7343	73.43
	5.00×10^{-4}	−341.0	392.4	90.06	130.8	179.30	0.7515	75.15
	7.50×10^{-4}	−408.2	160.2	104.3	98.42	73.19	0.8985	89.85
	10.00×10^{-4}	−421.5	127.7	105.2	117.5	58.33	0.9191	91.91
Salicin	1.00×10^{-4}	−358.1	404.5	95.02	126.8	184.80	0.7438	74.38
	2.50×10^{-4}	−387.3	261.2	99.86	108.8	119.40	0.8346	83.46
	5.00×10^{-4}	−395.1	152.2	93.91	97.1	69.54	0.9036	90.36
	7.50×10^{-4}	−407.3	108.4	94.35	101.3	49.53	0.9313	93.13
	10.00×10^{-4}	−399.7	61.57	89.28	96.66	28.13	0.9610	96.10

[a] E_{corr}, is the corrosion potential; i_{corr}, is the corrosion current density: β_a and β_c are Tafel constants for both anode and cathode; k, is the corrosion rate; θ, is the surface coverage; η_p, is the inhibition efficiency.

obtained were 58.33 mpy for Rhamnose and 28.13 mpy for Salicin. Both inhibitors exhibit good corrosion protection properties, with Salicin being more effective due to the nature of its structure. The results support that both Rhamnose and Salicin are effective and environmentally friendly corrosion inhibitors for carbon steel in acidic media.

3.1.2 Electrochemical frequency modulation (EFM) analysis. The intermodulation spectra of carbon steel in 1.0 M HCl, without and with different concentrations of Salicin and Rhamnose compounds at a temperature of 30 °C, are shown in Fig. 2 and S1, respectively. The occurrence of well-defined peaks at harmonic and intermodulation frequencies is used to confirm the integrity of the electrochemical frequency modulation (EFM) measurements.[42] The Blank Solution (1.0 M HCl) displays high current densities ($\log i$) across the frequency range, reflecting intense corrosion activity in the absence of inhibitors.[43] There is an appreciable reduction in current densities with increasing inhibitor concentrations, thus establishing the strong inhibitive action of Salicin and Rhamnose by significant adsorption on the steel surface.[44] Salicin shows a more intense and consistent decrease in intermodulation peak heights with increasing concentration compared to Rhamnose. This phenomenon suggests that Salicin forms a denser or more stable protective film on the metal surface. The suppression of intermodulation peaks reveals that the inhibitors interfere with both charge-transfer and diffusion-controlled corrosion processes.[45] EFM corrosion parameters are listed in Table 2. The results support and quantify the qualitative findings obtained from the intermodulation spectra. The Blank solution has the highest i_{corr} value, reflecting severe corrosion. With Rhamnose, i_{corr} is reduced from 467.3 to 140.5 μA cm^{-2} upon increasing concentration. A similar trend is obtained with Salicin, where i_{corr} is reduced from 437.4 to 126.1 μA cm^{-2}. The lowest i_{corr} was obtained with Salicin at a concentration of 10.00×10^{-4} M, verifying its higher inhibition capacity.[46] For both inhibitors, the parameters β_a and β_c change with concentration, indicating their effect on the anodic and cathodic reactions.[47] Importantly, Salicin causes sharper drops in both β_a and β_c at higher concentrations, reflecting stronger interference with the electrochemical kinetics. All Causality Factors (CF) values are within or close to the acceptable limit (theoretical CF-2 ≈ 2, CF-3 ≈ 3), confirming the validity of EFM measurements.[48] Corrosion rate decreased from 337.80 mpy (blank) to 64.19 mpy in the presence of 10.00×10^{-4} M Rhamnose (81.00% inhibition) and to 57.63 mpy in the presence of 10.00×10^{-4} M Salicin (82.94% inhibition). Both θ and η_{EFM}% increase regularly with inhibitor concentration.

3.1.3 Electrochemical impedance spectroscopy (EIS) analysis. Electrochemical Impedance Spectroscopy (EIS) was performed to evaluate the effectiveness of Rhamnose and Salicin as corrosion inhibitors for mild steel in 1.0 M HCl solution at 30 °C. The Nyquist, Bode, and phase angle plots are shown in Fig. 3, while the corresponding fitted parameters derived from the equivalent circuit model ($R_s(R_fCPE_f)(R_{ct}CPE_{dl})$) are provided in Table 3, as indicated in the insets of Fig. 3a and b. The Nyquist plots (Fig. 3a and b) of both inhibitors exhibit depressed semicircles, indicative of non-ideal capacitive behavior and surface heterogeneity[49] and hence better described by constant phase elements (CPEs) rather than ideal capacitors. To calculate the true capacitance using the CPE parameters, the following equation was used:[50]

$$C = \left(Y_0 R^{1-n}\right)^{\frac{1}{n}} \quad (3)$$

The semicircle diameter increases with an increase in inhibitor concentration, which is indicative of enhanced resistance to corrosion.[51] The equivalent circuit model used, which comprises two-time constants, one related to the surface film (R_f and CPE_f) and the other attributed to the charge transfer process (R_{ct} and CPE_{dl})[52] was found to exhibit excellent fitting accuracy, as evidenced from the low chi-squared (χ^2) values.[53] The solution resistance (R_s) showed minimal changes upon addition of the inhibitor, confirming that the changes in impedance are largely due to surface interactions and not bulk solution-related effects.[54] The film resistance (R_f) is the resistance of the inhibitor film developed on the steel surface, and

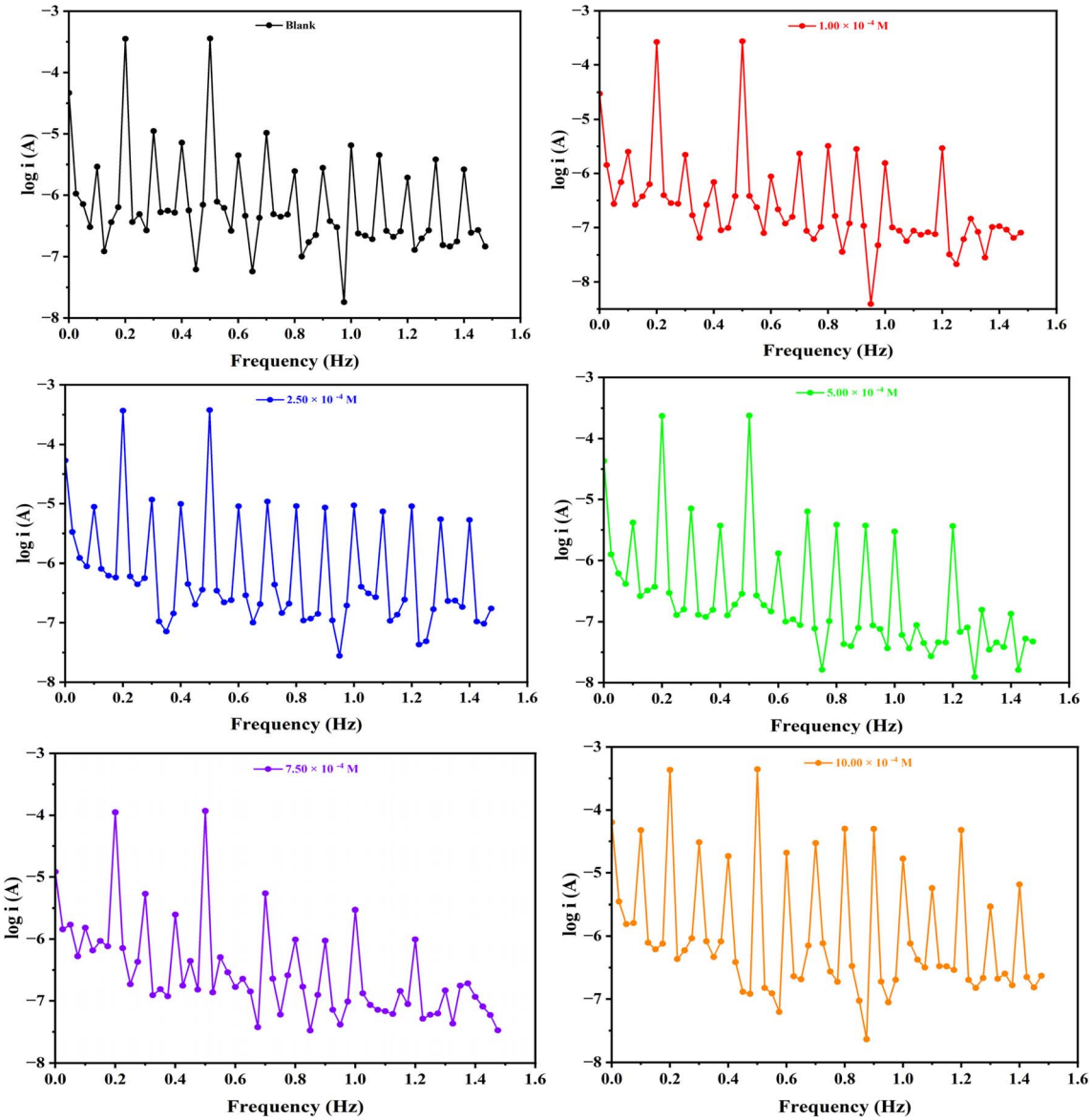

Fig. 2 Intermodulation spectra for carbon steel in 1.0 M HCl in absence and presence of different concentrations from Salicin compound at 30 °C.

the film capacitance (C_f) is the dielectric characteristic of the film layer. Both are important measures of the formation and protective quality of the inhibitor film.[55] With the addition of inhibitors, R_f increased significantly with concentration.[56] For Rhamnose, R_f rose from 8.04 Ω cm^2 at 1.00 × 10^{-4} M to a maximum of 66.99 Ω cm^2 at 7.50 × 10^{-4} M, suggesting progressive film formation. However, the slight reduction in R_f to 45.53 Ω cm^2 at 10.00 × 10^{-4} M could imply film restructuring, saturation, or minor desorption effects at high concentration. Salicin showed a more linear increase in R_f, from 4.65 Ω cm^2 to 76.67 Ω cm^2 over the same concentration range, suggesting stronger and more uniform film formation. This agrees with the generally higher inhibition efficiencies and R_{ct} values for Salicin than for Rhamnose. Concurrently, film capacitance (C_f) fell with rising inhibitor concentration for both inhibitors. This decrease indicates increasing film thickness or decreasing electricity due to the replacement of water molecules by the organic inhibitor film since capacitance is inversely proportional to film thickness[57] according to the Helmholtz model:[58]

$$C = \frac{\varepsilon\varepsilon_0 A}{d} \quad (4)$$

For example, C_f decreased from 199.40 mF cm^{-2} (Rhamnose at 1.00 × 10^{-4} M) to 20.96 mF cm^{-2} at 10.00 × 10^{-4} M, and for Salicin, from 211.08 to 20.68 mF cm^{-2}. This decrease in C_f corroborates the gradual development of a dense and insulating film that impedes charge and mass transfer at the metal/solution interface.[59] Globally, the concentration dependence of R_f and C_f confirms that both Rhamnose and Salicin develop protective surface films on the steel substrate, which are largely

Table 2 Electrochemical kinetic parameters[a] obtained by EFM technique for carbon steel in the absence and presence of various concentrations of (Rhamnose and Salicin) inhibitors in 1.0 M HCl at 30 °C

Inhibitor name	Conc. (M)	i_{corr} (μA cm^{-2})	β_a (mV dec^{-1})	β_c (mV dec^{-1})	CF-2	CF-3	k (mpy)	θ	η_{EFM}%
Blank	—	739.3	124.2	162.0	1.574	3.465	337.80	—	—
Rhamnose	1.00×10^{-4}	467.3	164.5	312.2	1.846	2.957	213.50	0.3679	36.79
	2.50×10^{-4}	410.3	164.3	254.8	1.844	2.218	187.50	0.4450	44.50
	5.00×10^{-4}	342.1	103.3	162.5	2.018	4.174	156.30	0.5373	53.73
	7.50×10^{-4}	242.6	49.5	56.2	1.170	2.449	110.80	0.6719	67.19
	10.00×10^{-4}	140.5	111.3	148.3	1.949	3.059	64.19	0.8100	81.00
Salicin	1.00×10^{-4}	437.4	108.9	115.5	2.013	3.079	199.90	0.4084	40.84
	2.50×10^{-4}	385.7	71.0	82.1	2.176	3.041	176.20	0.4783	47.83
	5.00×10^{-4}	307.7	84.9	100.0	2.008	3.114	140.60	0.5838	58.38
	7.50×10^{-4}	205.1	104.1	150.5	1.991	3.620	93.73	0.7226	72.26
	10.00×10^{-4}	126.1	34.8	41.7	1.714	3.294	57.63	0.8294	82.94

[a] E_{corr}, is the corrosion potential; i_{corr}, is the corrosion current density: β_a and β_c are Tafel constants for both anode and cathode; k, is the corrosion rate; θ, is the surface coverage; η_{EFM}, is the inhibition efficiency.

responsible for their corrosion inhibition efficiency. The higher R_f and lower C_f values for Salicin indicate the development of a denser and better adherent film in comparison to Rhamnose, in accordance with its greater protective effect. The charge transfer resistance (R_{ct}) and polarization resistance ($R_p = R_{ct} + R_f$) of the steel electrode increased noticeably with the introduction of both inhibitors, as compared to the blank solution. For example, R_{ct} was 19.05 Ω cm^2 in the absence of inhibitor. On addition of 10.0×10^{-4} M Rhamnose, R_{ct} reached 121.65 Ω cm^2, whereas the same concentration of Salicin caused it to increase to a much larger R_{ct} of 172.27 Ω cm^2, reflecting more efficient inhibition.[60] Likewise, the double-layer capacitance (C_{dl}), which is inversely proportional to the thickness of the electric double layer and the surface coverage, decreased with rising inhibitor concentration. This decrease in C_{dl} (from 406.90 μF cm^{-2} for blank to 70.90 μF cm^{-2} for Rhamnose and 85.83 μF cm^{-2} for Salicin at highest concentrations) attests to the adsorption of inhibitor molecules on the steel surface, which displaces water molecules and decreases the active surface area available for corrosion.[61] The inhibition efficiency (η_z) rose with concentration, reaching 88.60% for Rhamnose and 92.35% for Salicin at 10.0×10^{-4} M. This trend is concurrent with the rise in surface

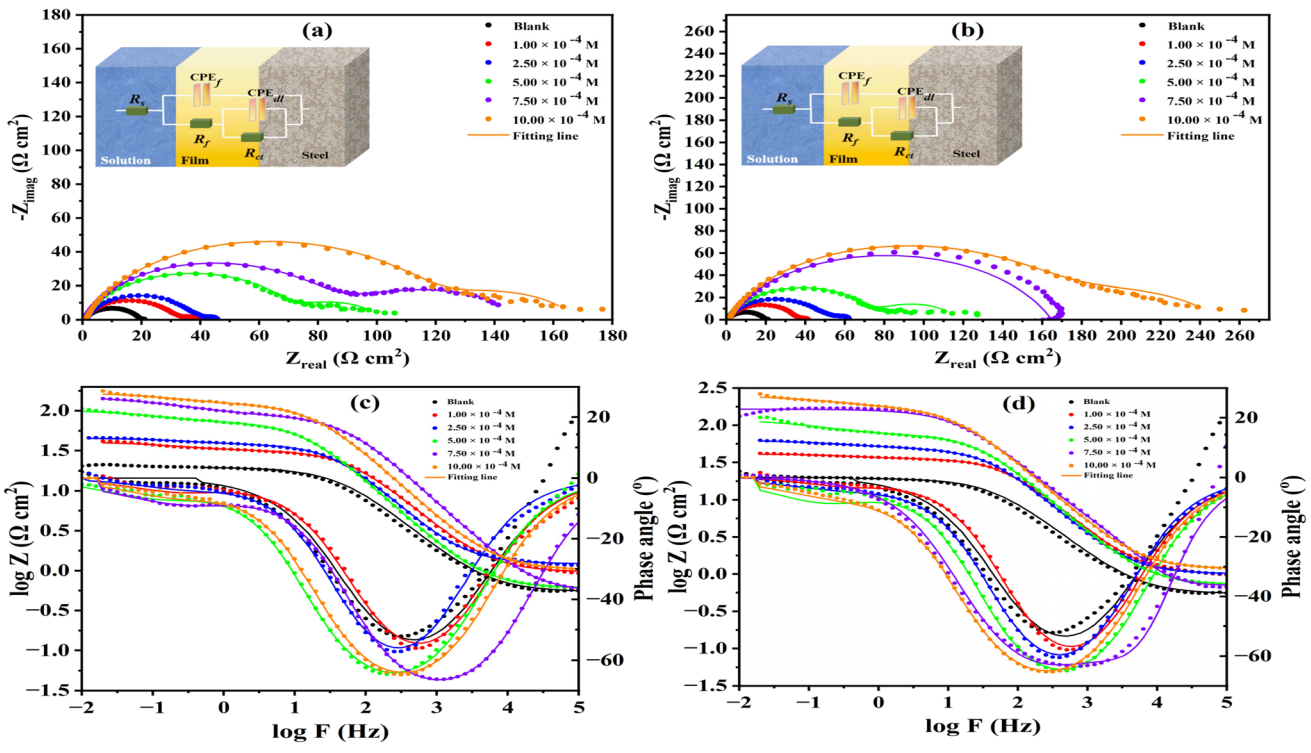

Fig. 3 Nyquist plots, bode and phase angle plots for steel in 1.0 M HCl solution without and with different concentrations of Rhamnose (a and c) and Salicin (b and d) compounds at 30 °C.

Table 3 EIS parameters for corrosion of steel in 1.0 M HCl in the absence and presence of different concentrations of Rhamnose and Salicin inhibitors at 30 °C[a]

Inhibitor	Conc. (M)	R_s (Ω cm^2)	R_f (Ω cm^2)	CPE_f		C_f (mF cm^{-2})	R_{ct} (Ω cm^2)	CPE_{dl}		C_{dl} (μF cm^{-2})	Chi squared (χ^2)	R_p ($R_f + R_{ct}$)	θ	η_z (%)
				Y_{o1} (mΩ^{-1} s^n cm^{-2})	n_1			Y_{o2} ($\mu\Omega^{-1}$ s^n cm^{-2})	n_2					
Blank	—	0.5409					19.05	736.27	0.8780	406.90	9.04×10^{-3}	19.05	—	—
Rhamnose	1.00×10^{-4}	0.9574	8.04	175.70	0.7320	199.40	31.21	460.05	0.8225	184.11	1.48×10^{-3}	39.25	0.5146	51.46
	2.50×10^{-4}	1.2178	6.91	121.70	0.7323	114.24	37.25	364.40	0.8294	150.48	9.28×10^{-4}	44.16	0.5686	56.86
	5.00×10^{-4}	0.6067	29.42	52.40	0.6866	63.84	71.92	362.62	0.8205	163.30	7.65×10^{-4}	101.34	0.8120	81.20
	7.50×10^{-4}	0.5437	66.99	35.11	0.6793	52.56	84.83	295.02	0.8343	141.83	1.34×10^{-4}	151.82	0.8745	87.45
	10.00×10^{-4}	1.0283	45.53	21.28	0.6786	20.96	121.65	166.96	0.8198	70.90	4.76×10^{-4}	167.18	0.8860	88.60
Salicin	1.00×10^{-4}	1.0008	4.65	211.80	0.8120	211.08	35.19	348.64	0.8253	137.35	7.64×10^{-4}	39.85	0.5219	52.19
	2.50×10^{-4}	1.0084	13.75	81.50	0.5984	87.98	48.05	385.83	0.8309	171.37	2.54×10^{-4}	61.80	0.6917	69.17
	5.00×10^{-4}	0.7234	42.06	47.14	0.6968	63.49	74.64	336.38	0.8338	161.38	1.89×10^{-3}	116.70	0.8367	83.67
	7.50×10^{-4}	0.7085	56.17	20.19	0.7263	21.17	107.99	282.69	0.8992	191.18	5.91×10^{-3}	164.16	0.8839	88.39
	10.00×10^{-4}	1.1769	76.67	18.04	0.7036	20.68	172.27	183.73	0.8194	85.83	3.70×10^{-3}	248.94	0.9235	92.35

[a] R_s = solution resistance, R_{ct} = charge transfer resistant, Y_0, n = constant phase elements, C_{dl} = double layer capacitance, θ = surface coverage, η_z = inhibition efficiency.

coverage (θ), demonstrating that the inhibitors efficiently adsorb on the steel surface and create a protective layer. As seen, Salicin consistently displayed slightly higher inhibition efficiency at all concentrations, implying a stronger or denser adsorption layer than Rhamnose. Bode and phase angle plots (Fig. 3c and d) confirm these findings. The $|Z|$ values at low frequencies rose with inhibitor concentration, and the phase angle maxima moved to more negative values, demonstrating enhanced barrier properties and greater capacitive behavior.[62,63] The wider and more negative phase angles with Salicin also imply better surface coverage and inhibition.

3.2 Adsorption isotherm studies

To achieve a deeper insight into the interaction between the inhibitor molecules and the steel surface, various adsorption isotherm models were used to examine the surface coverage data (θ) derived from electrochemical measurements. The main aim was to reveal the adsorption mechanism, determine binding strength, and establish the spontaneity of the adsorption process of the inhibitors.[64,65] The Langmuir isotherm model was mainly used to describe the monolayer adsorption behavior of inhibitors on the steel surface. Its linear form is given by:[66]

$$\frac{C}{\theta} = \frac{1}{K_{ads}} + C \quad (5)$$

As evident in Fig. 4 and Table 4, both Rhamnose and Salicin exhibited excellent linearity with regression coefficients (R^2) of 0.9911 and 0.9995, respectively. The slopes close to unity (0.9926 for Rhamnose and 1.0062 for Salicin) further attest that both inhibitors follow the Langmuir isotherm, meaning that the adsorption takes place through the formation of a uniform monolayer with negligible interaction among adsorbed species.[67] The K_{ads} values for each calculated from the intercepts were 7481 M^{-1} for Rhamnose and 9589 M^{-1} for Salicin (based on EIS data). The high values confirm strong adsorption of both inhibitors on the steel surface, with a higher binding affinity for

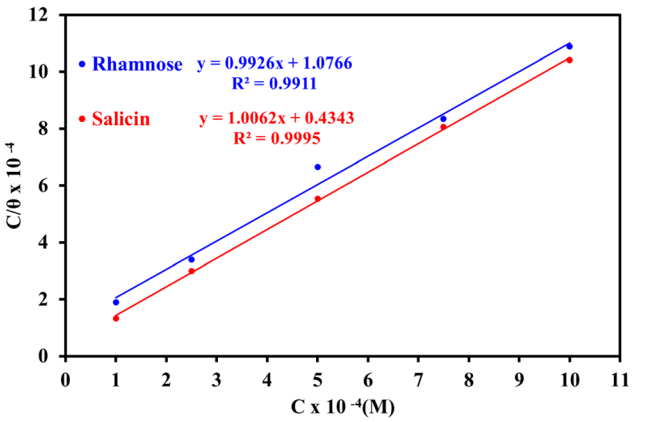

Fig. 4 The Langmuir adsorption model for Rhamnose and Salicin compounds on the steel in 1.0 M HCl at 30 °C.

Table 4 Adsorption isotherms models of the inhibitors with values of R^2, slopes, intercepts, K_{ads}, and ΔG_{ads} obtained by using data from electrochemical measurements[a]

Adsorption isotherm model	Linear form equation	Technique	Inhibitor	Slope	Intercept	R^2	K_{ads} (M^{-1})	ΔG_{ads} (kJ mol^{-1})
Freundlich	$\log\theta = \log K + 1/n \log C$	PDP	Rhamnose	0.23479	0.67542	0.93789	4.7361	−14.04
			Salicin	0.11073	0.31724	0.99425	2.0761	−11.96
Langmuir	$\frac{c}{\theta} = \frac{1}{K} + c$	EFM	Rhamnose	1.05979	0.00027	0.93687	3678	−30.80
			Salicin	1.04382	0.00023	0.95838	4334	−31.21
		EIS	Rhamnose	0.98756	0.00013	0.98969	7481	−32.59
			Salicin	0.98482	0.00010	0.99939	9589	−33.21
		PDP	Rhamnose	0.99256	0.00011	0.99108	9289	−33.13
			Salicin	1.00618	0.00004	0.99946	23023	−35.42
Frumkin	$\log\frac{\theta}{(1-\theta)C} = \log K + 2a\theta$	PDP	Rhamnose	0.09239	3.92853	0.01431	8.4827×10^3	−32.91
			Salicin	−0.55752	4.82566	0.30964	6.6937×10^4	−38.11
Temkin	$\theta = -\frac{1}{2a}\ln C - \frac{1}{2a}\ln K$	PDP	Rhamnose	5.67924	−12.19041	0.94337	0.1169	−4.71
			Salicin	10.63315	−17.14422	0.99771	0.1994	−6.06
Flory–Huggins	$\log\left(\frac{\theta}{c}\right) = \log K + n\log(1-\theta)$	PDP	Rhamnose	0.89662	3.92507	0.85440	8.4153×10^3	−32.89
			Salicin	1.08839	4.42560	0.94686	2.6644×10^4	−35.79
El-Awady	$\log\left(\frac{\theta}{1-\theta}\right) = \log K + y\log c$	PDP	Rhamnose	0.97717	3.92153	0.91216	10307.39	−33.40
			Salicin	0.88315	3.93997	0.95904	28924.01	−36.00

[a] R^2 = regression correlation coefficient, K = binding constant, θ = surface coverage, c = concentration.

Salicin compared to Rhamnose.[68] The free energy of adsorption (ΔG°_{ads}) was determined using the equation:

$$\Delta G_{ads} = -RT \ln 55.5 K_{ads} \quad (6)$$

The ΔG°_{ads} values calculated were −32.59 kJ mol^{-1} in the case of Rhamnose and −33.21 kJ mol^{-1} for Salicin (EIS-based data), which signify that the adsorption process was spontaneous and consists of mixed physisorption and chemisorption.[69] ΔG°_{ads} values in the range of −20 to −40 kJ mol^{-1} usually imply that the adsorption comprises both electrostatic (physical) and covalent (chemical) interactions.[70] In order to further validate the adsorption nature, various additional isotherm models *i.e.*, Freundlich, Frumkin, Temkin, Flory–Huggins, and El-Awady—were tested using the PDP data (see Table 4). Although some models (*e.g.*, Temkin and El-Awady) attained high R^2 values (*i.e.*, R^2 = 0.99771 for Temkin–Salicin and 0.95904 for El-Awady–Rhamnose), the Langmuir model universally showed the best fit across methods and displayed theoretical agreement with empirically observed monolayer behavior. For all models, El-Awady and Flory–Huggins also provided thermodynamically reasonable ΔG°_{ads} values (*e.g.*, −35.42 and −36.00 kJ mol^{-1} for Salicin), supporting the mixed adsorption mechanism and relatively strong surface binding.[71] Both the binding constants K_{ads} and ΔG°_{ads} values continually indicated a stronger affinity of Salicin for the steel surface compared to Rhamnose, independent of the isotherm model. The stronger affinity is obviously caused by the greater number of active adsorption sites (the aromatic benzene ring and the phenolic –OH group) and hence more efficient surface coverage and greater inhibition efficiency.

3.3 Molecular aspects analysis

The corrosion inhibition efficiency of organic molecules such as Salicin and Rhamnose is closely tied to their ability to adsorb onto the metal surface, forming a protective layer that mitigates corrosive attack. This adsorption process is fundamentally influenced by the electronic structure of the inhibitor, particularly the distribution of atomic charges. Atoms with higher negative charges are more likely to donate electrons to the metal surface, enhancing adsorption strength and, consequently, inhibition performance.[72] In this study, atomic charges were calculated using three population analysis methods – Hirshfeld, Electrostatic Potential (ESP), and Natural Bond Orbital (NBO) – to identify potential adsorption centers (Table 5). Hirshfeld charges are derived from partitioning the electron density relative to a reference pro-atom and tend to be less sensitive to molecular environment. ESP charges are obtained by fitting the molecular electrostatic potential and reflect how the molecule interacts with external electric fields. NBO charges, which are based on localized orbitals, provide a chemically intuitive picture of electron distribution and are particularly useful for identifying donor–acceptor interactions.[73] To ensure consistency with subsequent analyses, including Fukui indices and natural bond orbital interactions, the atomic charges in Table 5 were ordered according to NBO values. This approach highlights the most reactive sites in each molecule. For instance, Salicin exhibits several oxygen atoms with highly negative NBO charges – O_6 (−0.781), O_7 (−0.780), and O_5 (−0.768) – suggesting strong electron-donating potential. In contrast, Rhamnose shows slightly fewer and less diverse adsorption-active centers, with O_2 (−0.783), O_3 (−0.782), and O_4 (−0.776) being the most negatively charged. These findings support the hypothesis that Salicin, due to its larger molecular size, additional phenyl ring, and greater number of oxygen atoms, may offer superior adsorption and thus enhanced corrosion inhibition compared to Rhamnose. The atomic charge analysis not only provides insight into molecular reactivity but also serves as a predictive tool for evaluating the performance of corrosion inhibitors prior to experimental validation.

Table 5 Hirshfeld, ESP and NBO atomic charges of Rhamnose and Salicin molecules

Rhamnose				Salicin			
Atoms[a]	Hirshfeld	ESP	NBO	Atoms	Hirshfeld	ESP	NBO
O_5	−0.224	−0.786	−0.786	O_3	−0.25	−0.616	−0.781
O_2	−0.259	−0.783	−0.783	O_6	−0.265	−0.683	−0.781
O_3	−0.23	−0.782	−0.782	O_7	−0.258	−0.658	−0.78
O_4	−0.254	−0.776	−0.776	O_4	−0.226	−0.61	−0.774
C_{11}	−0.087	−0.711	−0.711	O_5	−0.242	−0.65	−0.768
O_1	−0.183	−0.615	−0.615	O_1	−0.136	−0.166	−0.626
C_8	0.041	0.03	0.03	O_2	−0.15	−0.347	−0.563
C_7	0.039	0.038	0.038	C_{16}	−0.053	−0.251	−0.281
C_6	0.034	0.047	0.047	C_{20}	−0.046	−0.155	−0.25
C_9	0.046	0.051	0.051	C_{19}	−0.038	−0.101	−0.232
C_{10}	0.117	0.365	0.365	C_{17}	−0.04	−0.139	−0.218
—	—	—	—	C_{15}	−0.018	−0.199	−0.116
—	—	—	—	C_{18}	0.026	0.35	−0.116
—	—	—	—	C_{13}	0.023	0.356	−0.113

[a] Atom numbering is listed in Fig. S2.

While atomic charge analysis provides valuable insight into the static electron distribution within a molecule, Fukui functions offer a more dynamic and realistic perspective on molecular reactivity, particularly in the context of corrosion inhibition. Unlike atomic charges, which are fixed and represent the equilibrium state of electron density, Fukui functions describe how the local electron density responds to external perturbations such as an electric field or the presence of a metal surface. This makes them especially relevant for modeling adsorption behavior, as they simulate the actual interaction conditions between inhibitor molecules and the metal substrate. In practice, calculating Fukui functions directly from electron density derivatives can be computationally intensive. Therefore, in this study, we adopted the finite difference approximation using NBO atomic charges, which provides a simpler yet effective method for estimating Fukui indices.[74] This approach allowed us to identify nucleophilic sites f^-, electrophilic sites f^+, and regions of dual reactivity Δf across the molecular structure. The atomic charge analysis remains foundational to this process, as it supplies the baseline data from which Fukui indices are derived. Specifically, we relied on NBO atomic charges to ensure consistency with other sections of the study, including orbital interaction analysis and donor–acceptor evaluations. To emphasize the electron-donating potential of the inhibitors, which is critical for adsorption onto the positively charged metal surface, we ordered the Fukui indices in Table 6 according to their negative Fukui values f^-. This highlights the most nucleophilic centers in each molecule. For example, in Salicin, C_{20} ($f^- = 0.1859$), C_{14} ($f^- = 0.1454$), and O_2 ($f^- = 0.083$) exhibit strong nucleophilic character, suggesting high potential for electron donation and surface interaction. In comparison, Rhamnose shows similarly reactive sites such as O_1 ($f^- = 0.1722$), O_2 ($f^- = 0.1547$), and O_3 ($f^- = 0.1502$), but with slightly lower diversity and intensity. These findings reinforce the earlier conclusion that Salicin, due to its extended conjugation and additional reactive centers, may exhibit superior adsorption and corrosion inhibition performance. Overall, the Fukui index analysis complements the atomic charge data and enhances our understanding of how molecular structure influences inhibitor efficiency under realistic electrochemical conditions.

Natural Bond Orbital (NBO) analysis is a powerful quantum chemical tool that provides a localized and chemically intuitive description of molecular electronic structure. Unlike Frontier Molecular Orbital (FMO) analysis, which focuses on the highest occupied and lowest unoccupied molecular orbitals (HOMO and LUMO) and their energy levels, NBO analysis decomposes the electron density into natural atomic hybrids and bonding interactions, revealing donor–acceptor relationships and orbital contributions with high precision.[75] This method is particularly valuable in corrosion inhibition studies, as it identifies the specific atoms and orbitals responsible for electron donation to the metal surface, thereby facilitating adsorption. In this study, NBO analysis reveals distinct electronic characteristics for Rhamnose and Salicin (Table 7). The corresponding NBO orbital diagrams are illustrated in Fig. S3 and S4. For Rhamnose, the orbitals from HOMO to HOMO−4 are dominated by lone pairs on oxygen atoms, such as LP(2)O_2 (occupancy = 1.95755, energy = −0.29005 a.u.) and LP(2)O_4 (occupancy = 1.95235, energy = −0.29359 a.u.), all exhibiting nearly pure p-character (≈99.9%). This indicates strong localization of electron density on oxygen atoms, consistent with their high negative atomic charges and nucleophilic Fukui indices. In contrast, Salicin's HOMO to HOMO−2 orbitals are primarily composed of π-bonding interactions within the conjugated phenyl system, such as BD(2)C_{15}–C_{17} (occupancy = 1.65838, energy = −0.24674 a.u.), BD(2)C_{19}–C_{20} (1.66161, −0.24777 a.u.), and BD(2)C_{14}–C_{16} (1.67254, −0.26080 a.u.). These orbitals have lower electron occupancy and are delocalized across the aromatic ring, suggesting enhanced reactivity and surface interaction potential. Interestingly, while oxygen atoms dominate in terms of static negative atomic charges, the phenyl

Table 6 Fukui indices derived using NBO atomic charges for Rhamnose and Salicin molecules

Rhamnose				Salicin			
Atoms	f^-	f^+	Δf	Atoms	f^-	f^+	Δf
O_1	0.1722	0.017	−0.1552	C_{20}	0.1859	0.0039	−0.182
O_2	0.1547	0.0122	−0.1425	C_{14}	0.1454	0.0005	−0.1449
O_3	0.1502	0.0052	−0.1449	C_{15}	0.1018	0.131	0.0291
O_4	0.1003	0.0232	−0.0772	O_2	0.083	0.0133	−0.0697
O_5	0.0251	0.104	0.079	C_{19}	0.0751	0.1595	0.0844
C_7	0.0066	−0.003	−0.0036	O_7	0.0563	0.0326	−0.0237
C_9	0.0042	−0.0056	0.0013	C_{16}	0.0281	0.1745	0.1464
C_8	0.0007	0.0053	0.0046	O_6	0.0189	0.0021	−0.0168
C_{11}	−0.0067	−0.0009	−0.0058	O_5	0.0171	0.0027	−0.0145
C_6	−0.0086	0.0058	−0.0027	O_4	0.0136	0.0021	−0.0115
C_{10}	−0.0137	0.0398	0.0261	O_3	0.0121	0.0017	−0.0104
—	—	—	—	O_1	0.0081	−0.0017	−0.0064
—	—	—	—	C_{17}	0.0056	0.1846	0.1789

carbons in Salicin show superior responsiveness in Fukui analysis indicating dynamic electron donation capability. This duality is confirmed by the NBO orbital analysis, where the π-orbitals of carbon atoms occupy the upper energy levels, followed by oxygen lone pairs. These findings underscore the complementary roles of oxygen and carbon centers in corrosion inhibition: oxygen atoms provide strong localized electron density for initial adsorption, while conjugated carbon systems enhance surface interaction through delocalized π-electron donation. Together, the NBO and Fukui analyses offer a comprehensive picture of molecular reactivity, supporting the hypothesis that Salicin's structural complexity and electronic versatility make it a more effective corrosion inhibitor than Rhamnose.

Natural Bond Orbital (NBO) donor–acceptor analysis provides a quantitative measure of intramolecular electron delocalization, which plays a crucial role in enhancing the reactivity and adsorption behavior of corrosion inhibitors (Table 8). These interactions are characterized by stabilization energies (E^2), which reflect the strength of electron donation from a filled donor orbital to an empty acceptor orbital. In the context of corrosion inhibition, such delocalization facilitates the redistribution of electron density, allowing the molecule to better interact with the metal surface. In Rhamnose, the most prominent interactions involve lone pairs on oxygen atoms donating to antibonding orbitals, such as LP(2)O_5 → BD*(1)O_1–C_{10} with E^2 = 15.35 kcal mol^{-1}, and LP(2)O_1 → BD*(1)O_5–C_{10} with E^2 = 11.5 kcal mol^{-1}. These values confirm the strong electron-donating capability of oxygen atoms, consistent with

Table 7 Natural bond orbitals from HOMO to HOMO−8 of Rhamnose and Salicin molecules

NBOs	Occ.	Energy	Hybrids	s%	p%	s%	p%
Rhamnose molecule							
LP(2)O_2	1.95755	−0.29005	$p^{99.99}$	0.32	99.96	—	—
LP(2)O_4	1.95235	−0.29359	$p^{1.00}$	0.00	99.91	—	—
LP(2)O_1	1.90058	−0.30380	$p^{99.99}$	0.49	99.45	—	—
LP(2)O_5	1.92736	−0.31210	$p^{99.99}$	0.84	99.08	—	—
LP(2)O_3	1.94803	−0.31577	$p^{49.02}$	2.00	97.93	—	—
BD(1)C_{11}–H_{19}	1.98751	−0.49413	$0.7907p^{3.12} + 0.6122s$	24.29	75.66	99.95	0.05
BD(1)C_{11}–H_{17}	1.98945	−0.49431	$0.7879p^{3.18} + 0.6158s$	23.94	76.01	99.95	0.05
BD(1)C_{11}–H_{18}	1.98288	−0.49629	$0.7888p^{3.19} + 0.6146s$	23.88	76.07	99.95	0.05
BD(1)C_6–H_{12}	1.97298	−0.49866	$0.7888p^{3.07} + 0.6146s$	24.57	75.37	99.95	0.05
Salicin molecule							
BD(2)C_{15}–C_{17}	1.65838	−0.24674	0.7146p + 0.6995p	0.00	99.96	0.00	99.96
BD(2)C_{19}–C_{20}	1.66161	−0.24777	0.7026p + 0.7115p	0.00	99.96	0.00	99.96
BD(2)C_{14}–C_{16}	1.67254	−0.26080	0.7059p + 0.7083p	0.02	99.94	0.01	99.94
LP(2)O_6	1.95354	−0.29134	$p^{99.99}$	0.40	99.52	—	—
LP(2)O_7	1.95070	−0.29180	$p^{99.99}$	0.32	99.61	—	—
LP(2)O_3	1.95553	−0.29692	$p^{99.99}$	0.04	99.88	—	—
LP(2)O_5	1.94845	−0.30091	$p^{99.99}$	0.04	99.88	—	—
LP(2)O_4	1.94411	−0.31316	$p^{99.99}$	0.39	99.53	—	—
LP(2)O_1	1.92888	−0.32322	$p^{99.99}$	0.11	99.84	—	—
LP(2)O_2	1.89340	−0.34017	$p^{26.57}$	3.62	96.30	—	—

Table 8 Selected NBO donor–acceptor interactions[a] within Rhamnose and Salicin molecules

Donor NBO (i)	Acceptor NBO (j)	$E^{(2)}$ (kcal mol^{-1})	$E_{(j)} - E_{(i)}$ (a.u.)	$F_{(i,j)}$ (a.u.)
Rhamnose				
LP(2)O_5	BD*(1)O_1–C_{10}	15.35	0.6	0.086
LP(2)O_1	BD*(1)O_5–C_{10}	11.5	0.61	0.075
LP(2)O_4	BD*(1)C_6–C_8	8.3	0.67	0.067
LP(2)O_3	BD*(1)C_7–C_9	8.27	0.69	0.067
LP(2)O_2	BD*(1)C_6–H_{12}	6.79	0.74	0.064
LP(2)O_2	BD*(1)C_6–C_7	5.62	0.67	0.055
LP(2)O_1	BD*(1)C_9–H_{15}	5.36	0.77	0.058
LP(2)O_1	BD*(1)C_7–C_9	4.78	0.67	0.051
BD(1)C_6–H_{12}	BD*(1)O_4–C_8	4.58	0.79	0.054
LP(2)O_1	BD*(1)C_8–C_{10}	4.53	0.66	0.05
Salicin				
BD*(2)C_{14}–C_{16}	BD*(2)C_{15}–C_{17}	274.21	0.01	0.083
BD(2)C_{15}–C_{17}	BD*(2)C_{14}–C_{16}	22.32	0.27	0.07
BD(2)C_{19}–C_{20}	BD*(2)C_{15}–C_{17}	21.12	0.28	0.069
BD(2)C_{19}–C_{20}	BD*(2)C_{14}–C_{16}	20.2	0.27	0.067
BD(2)C_{14}–C_{16}	BD*(2)C_{19}–C_{20}	19.99	0.29	0.069
BD(2)C_{15}–C_{17}	BD*(2)C_{19}–C_{20}	19.66	0.28	0.066
BD(2)C_{14}–C_{16}	BD*(2)C_{15}–C_{17}	19.09	0.3	0.068
LP(2)O_2	BD*(1)O_1–C_{12}	13.48	0.62	0.082
LP(1)O_1	BD*(1)O_7–H_{38}	12.88	1.06	0.105
LP(2)O_5	BD*(1)C_{10}–C_{12}	8.29	0.66	0.066

[a] BD: bonding orbital. BD*: antibonding orbital, LP: lone pair orbital, RY*: Rydberg orbital.

their dominance in atomic charge and HOMO orbital analysis. Conversely, Salicin exhibits a different electronic behavior, where the highest stabilization energies arise from π–π* interactions within its conjugated phenyl system. Notably, BD(2)C_{14}–C_{16} → BD*(2)C_{15}–C_{17} shows an exceptionally high E^2 = 274.21 kcal mol^{-1}, followed by BD(2)C_{15}–C_{17} → BD* (2)C_{14}–C_{16} with E^2 = 22.32 kcal mol^{-1}, and BD(2)C_{19}–C_{20} → BD*(2)C_{15}–C_{17} with E^2 = 21.12 kcal mol^{-1}. These interactions highlight the delocalized nature of the π-electron system in Salicin, which complements the Fukui analysis where carbon atoms showed high nucleophilic reactivity. The presence of both localized lone pairs and delocalized π-systems in Salicin suggests a synergistic mechanism for corrosion inhibition: oxygen atoms provide strong initial adsorption through localized electron donation, while the phenyl ring enhances surface stabilization *via* π-d orbital overlap with the iron surface. Thus, Table 8 reinforces the conclusion that Salicin's structural and electronic complexity enables more effective interaction with the metal surface compared to Rhamnose, supporting its observed superior inhibition performance.

To gain a comprehensive understanding of the electronic behavior of Salicin and Rhamnose as corrosion inhibitors, we evaluated their global reactivity descriptors in both the gas phase and aqueous medium (Table 9) and visualized their HOMO and LUMO isosurfaces (Fig. 5). Performing calculations in both media allows us to simulate the inhibitors' behavior under different environmental conditions. While gas-phase data provides intrinsic molecular properties, aqueous-phase results better reflect the realistic corrosion environment, where water and ions influence molecular reactivity and adsorption dynamics. Among the key descriptors, the HOMO energy indicates the molecule's ability to donate electrons to the metal surface, while the LUMO energy reflects its capacity to accept back-donated electrons from the metal.[76] A higher HOMO and lower LUMO energy generally enhance adsorption. In aqueous phase, Salicin exhibits a HOMO energy of −6.702 eV and LUMO energy of −0.381 eV, while Rhamnose shows HOMO of −7.019 eV and LUMO of 1.748 eV. The significantly lower LUMO energy in Salicin suggests a stronger capacity for back-donation, while its higher HOMO energy indicates better electron-donating ability. Furthermore, Salicin has a smaller energy gap (ΔE = 6.321 eV) compared to Rhamnose (ΔE = 8.767 eV), implying greater chemical reactivity and a more favorable interaction with the metal surface.[77] The global descriptors further support this conclusion. Salicin shows higher electronegativity (χ = 3.541) and more negative chemical potential (μ = −3.541), indicating a stronger tendency to attract electrons. Its chemical hardness (η = 3.16 eV) and softness (σ = 0.316 eV^{-1}) suggest moderate reactivity, while the global electrophilicity index (ω = 1.984 eV) reflects its ability to stabilize charge transfer during adsorption. Additionally, Salicin exhibits a higher fraction of electron transfer (ΔN = 0.943) compared to Rhamnose (ΔN = 0.783), reinforcing its superior electron exchange capability with the metal surface.

The spatial distribution of the frontier orbitals, as shown in Fig. 5, adds another layer of insight. In Salicin, both the HOMO and LUMO are localized over the phenyl ring, indicating that the conjugated π-system plays a dominant role in both electron donation and back-donation. This delocalization enhances the molecule's ability to interact with the metal surface through π-d orbital overlap. In contrast, Rhamnose shows HOMO and LUMO localized on oxygen atoms, suggesting that its reactivity is primarily governed by lone pair interactions. This difference in orbital localization aligns with earlier findings from Fukui and NBO analyses, reinforcing the conclusion that Salicin's extended conjugation and dual reactivity centers make it a more versatile and effective corrosion inhibitor.

The Molecular Electrostatic Potential (MEP) maps of Rhamnose and Salicin offer valuable insight into the spatial distribution of electron density, helping to visualize the regions most likely to interact with the metal surface during corrosion inhibition (Fig. 5). In Rhamnose, the MEP map reveals intense red regions concentrated around the oxygen atoms, indicating zones of high negative electrostatic potential. These areas correspond to the molecule's nucleophilic centers, as confirmed by atomic charge analysis and Fukui indices. The localization of both HOMO and LUMO orbitals on these oxygen atoms further supports their role in electron donation and back-donation, making them the primary sites for adsorption onto the metal surface. In contrast, Salicin's MEP map displays a more delocalized electrostatic profile, with negative potential regions not only around oxygen atoms but also extending across the phenyl ring. This broader distribution reflects the molecule's conjugated π-system, which plays a significant role in surface

Table 9 The calculated global reactivity indices of Rhamnose and Salicin inhibitors in different medium

	Rhamnose		Salicin	
Molecular parameters	Gas phase	Aqueous	Gas phase	Aqueous
E_{LUMO}	1.377	1.748	−0.377	−0.381
E_{HOMO}	−6.886	−7.019	−6.68	−6.702
ΔE	8.263	8.767	6.303	6.321
Ionization potential (I)	6.886	7.019	6.68	6.702
Electron affinity (A)	−1.377	−1.748	0.377	0.381
Electronegativity (χ)	2.755	2.636	3.529	3.541
Chemical potential (μ)	−2.755	−2.636	−3.529	−3.541
Chemical hardness (η)	4.132	4.384	3.152	3.16
Chemical softness (σ)	0.242	0.228	0.317	0.316
Global electrophilicity index (ω)	0.919	0.792	1.976	1.984
Fraction of electron transferred (ΔN)	0.816	0.783	0.947	0.943

interaction. The HOMO and LUMO isosurfaces of Salicin are both localized on the phenyl ring, indicating that π-electrons are actively involved in both donation and acceptance processes. This delocalization enhances the molecule's ability to engage in π-d orbital overlap with the iron surface, contributing to stronger and more stable adsorption. The contrast between the two MEP maps highlights the localized reactivity of Rhamnose *versus* the dual and delocalized reactivity of Salicin.

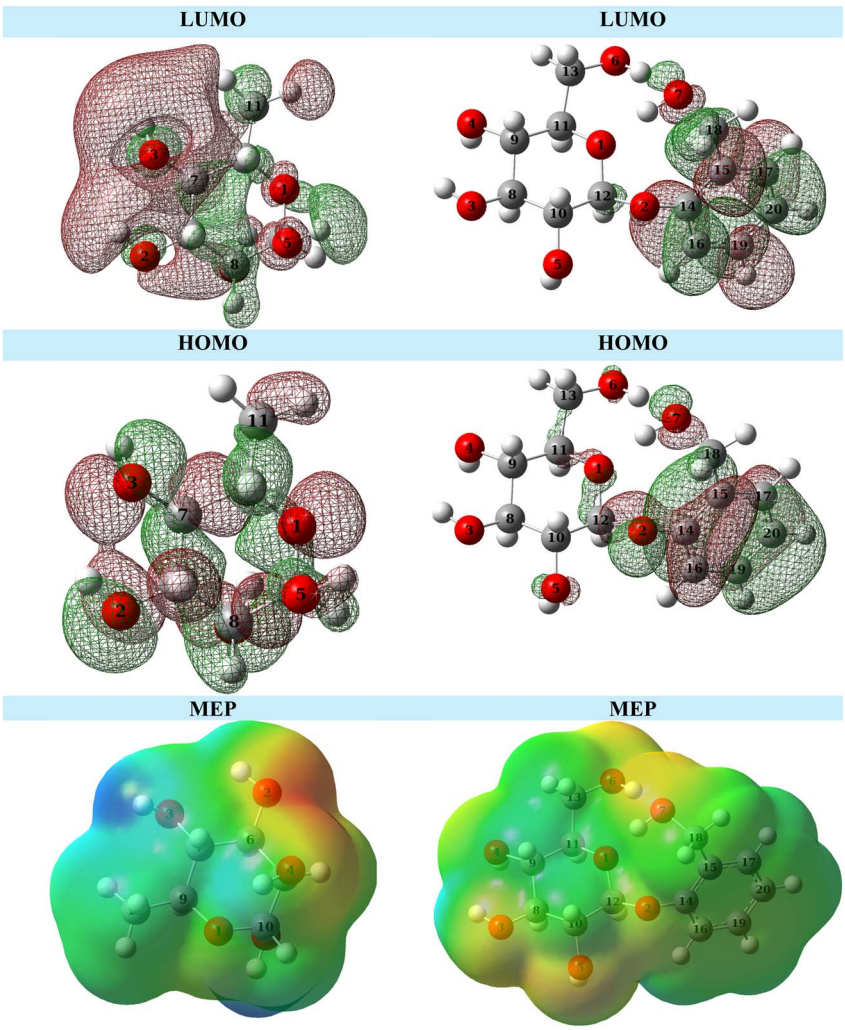

Fig. 5 The frontier molecular orbitals and MEP of Rhamnose (left) and Salicin (right).

While Rhamnose relies heavily on lone pair donation from oxygen atoms, Salicin benefits from both oxygen lone pairs and aromatic π-electrons, offering a more versatile interaction profile. These findings collectively confirm that Salicin's structural and electronic features make it a more effective corrosion inhibitor under realistic aqueous conditions.

3.4 Adsorption energy analysis

The adsorption locator analysis provides quantitative insight into the interaction strength between the inhibitor molecules and the Fe(110) surface (Fig. 6). The adsorption energy is a critical parameter reflecting the thermodynamic favorability of the adsorption process.[78] A more negative value indicates stronger binding and greater inhibition potential. Salicin exhibits a significantly more negative adsorption energy (−230.86 kcal mol^{-1}) compared to Rhamnose (−83.58 kcal mol^{-1}), suggesting a much stronger interaction with the iron surface (Table 10). This is consistent with the molecule's extended π-conjugation and multiple oxygen atoms, which facilitate both π-d orbital overlap and lone pair donation, enhancing both physisorption and chemisorption mechanisms. The rigid adsorption energy, which excludes molecular deformation, also favors Salicin (−142.00 kcal mol^{-1} *vs.* −72.54 kcal mol^{-1}), indicating that even without structural rearrangement, Salicin binds more effectively. However, the deformation energy of Salicin (−88.86 kcal mol^{-1}) is substantially higher than that of Rhamnose (−11.04 kcal mol^{-1}), reflecting the structural flexibility and adaptability of Salicin during adsorption. This flexibility may contribute to its ability to form more stable and extensive interactions with the metal surface. The dE_{ads}/dN_i values, which represent the adsorption energy per interacting atom, further confirm Salicin's superior performance, reinforcing its role as a more efficient green corrosion inhibitor. These findings align with the theoretical predictions from DFT, NBO, and Fukui analyses, and support the conclusion that Salicin's molecular architecture and electronic properties make it a more potent inhibitor for carbon steel in 1 M HCl.

Table 10 Calculated adsorption locator outputs for most stable configurations of Rhamnose and Salicin inhibitors

Parameter	Rhamnose	Salicin
Total energy (kcal mol^{-1})	−49.737	−82.336
Adsorption energy (kcal mol^{-1})	−83.577	−230.860
Rigid adsorption energy (kcal mol^{-1})	−72.538	−142.000
Deformation energy (kcal mol^{-1})	−11.039	−88.860
dE_{ads}/dN_i (kcal mol^{-1})	−83.577	−230.860

3.5 Corrosion mechanism

The corrosion inhibition of carbon steel in 1 M HCl by Rhamnose and Salicin proceeds through a multi-pathway adsorption mechanism involving electrostatic interactions, electron donation, and back-donation, each contributing to the formation of a protective molecular layer on the metal surface (Fig. 7). Initially, electrostatic attraction plays a key role in guiding the inhibitor molecules toward the positively charged steel surface. Both Rhamnose and Salicin possess multiple oxygen atoms with high negative atomic charges (as shown by NBO and ESP analyses), which interact favorably with the metal surface. This interaction is particularly pronounced in acidic media, where the steel surface is protonated and thus electropositive. Upon approaching the surface, electron donation from the inhibitor to the metal occurs primarily through lone pairs on oxygen atoms. In Rhamnose, the HOMO orbitals are localized on these oxygen atoms, facilitating direct donation into vacant d-orbitals of iron. Salicin, while also rich in oxygen atoms, exhibits an additional pathway *via* its conjugated π-system, where delocalized electrons from the phenyl ring contribute to surface

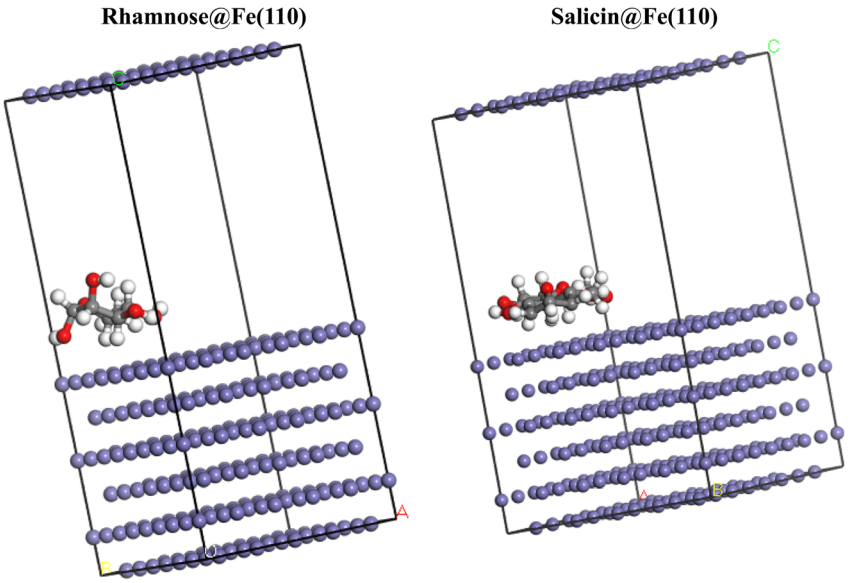

Fig. 6 Favorable configurations of Rhamnose@Fe(110) and Salicin@Fe(110) complexes.

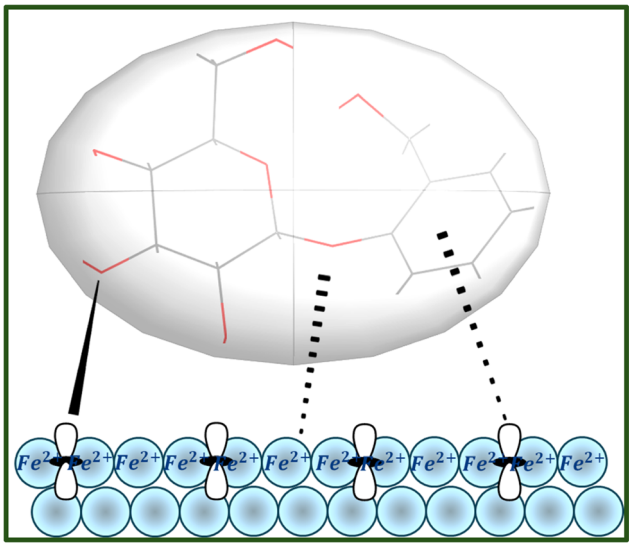

Fig. 7 The suggested corrosion mechanism through back donation (right dashed wedge), electron donation (solid wedge) and electrostatic attraction (left dashed wedge).

binding through π-d orbital overlap. This dual donation mechanism enhances Salicin's adsorption strength and surface coverage. Simultaneously, back-donation from the metal to the inhibitor is enabled by the LUMO orbitals. Salicin's LUMO is energetically lower and spatially aligned with the phenyl ring, allowing efficient acceptance of electron density from the metal surface. This stabilizes the adsorption complex and reinforces chemisorption. In contrast, Rhamnose's LUMO is localized on oxygen atoms and lies at a higher energy level, making back-donation less favorable. These synergistic effects result in the formation of a stable, protective layer that impedes the access of corrosive species to the metal surface, with Salicin demonstrating superior performance due to its electronic versatility and structural complexity.

4. Conclusion

This study demonstrates the effectiveness of Rhamnose and Salicin as environmentally friendly corrosion inhibitors for carbon steel in acidic media. Through a combination of electrochemical techniques and quantum chemical modeling, Salicin was found to outperform Rhamnose in terms of inhibition efficiency, adsorption strength, and electronic reactivity. The integration of DFT, NBO, Fukui indices, and adsorption simulations provided deep insights into the molecular mechanisms governing inhibitor performance. The findings underscore the importance of molecular-level understanding in the rational design of green inhibitors and position Salicin as a promising candidate for sustainable corrosion protection in industrial applications.

Author contributions

F. A. A. and M. A. A.: investigation; resources; data curation; computations. M. A. B. and A. M. A.: investigation; analysis; writing – original draft.

Conflicts of interest

The authors declare that they have no known competing financial interests or personal relationships that could have appeared to influence the work reported in this paper.

Data availability

The datasets supporting the findings of this study are available from the authors upon reasonable request.

The supporting information (SI) file provides additional data to support the findings of this study. Supplementary information: electrochemical data (intermodulation spectra) for the Rhamnose inhibitor; computational chemistry results, including the optimized molecular structures of the investigated inhibitors (Rhamnose and Salicin) and visualizations of their key Natural Bond Orbitals (NBOs). See DOI: https://doi.org/10.1039/d5ra06243h.

Acknowledgements

The authors are thankful to the Deanship of Graduate Studies and Scientific Research at the University of Bisha for supporting this work through the Fast-Track Research Support Program.

References

1 M. A. Bedair, A. M. Abuelela, W. M. Zoghaib and T. A. Mohamed, Molecular structure, tautomer's, reactivity and inhibition studies on 6-Methyl-2-thiouracil for mild steel corrosion in aqueous HCl (1.00 M): Experimental and Theoretical Studies, *J. Mol. Struct.*, 2021, **1244**, 130927, DOI: 10.1016/j.molstruc.2021.130927.

2 M. A. Mostafa, A. M. Ashmawy, M. A. M. A. Reheim, M. A. Bedair and A. M. Abuelela, Molecular structure aspects and molecular reactivity of some triazole derivatives for corrosion inhibition of aluminum in 1 M HCl solution, *J. Mol. Struct.*, 2021, **1236**, 130292, DOI: 10.1016/j.molstruc.2021.130292.

3 A. M. Abuelela, M. A. Bedair, W. M. Zoghaib, L. D. Wilson and T. A. Mohamed, Molecular structure and mild steel/HCl corrosion inhibition of 4,5-Dicyanoimidazole: Vibrational, electrochemical and quantum mechanical calculations, *J. Mol. Struct.*, 2021, **1230**, 129647, DOI: 10.1016/j.molstruc.2020.129647.

4 A. Ahmed, O. B. Chanu, A. Koch and R. A. Lal, Synthesis, spectroscopic and electrochemical characterisation of binuclear dioxomolybdenum complexes derived from disalicylaldehyde succinoyldihydrazone, *J. Mol. Struct.*, 2012, **1029**, 161–168, DOI: 10.1016/j.molstruc.2012.06.053.

5 M. A. Bedair, Q. A. Yousif, Z. Fadel, S. Melhi, F. A. Al-Odail and A. M. Abuelela, Experimental and theoretical analyses of the corrosion inhibition efficacy of new penicillanic acid derivatives for carbon steel in hydrochloric acid environment, *J. Mol. Struct.*, 2025, **1328**, 141282, DOI: 10.1016/j.molstruc.2024.141282.

6 Q. A. Yousif, M. A. Bedair, A. M. Abuelela, A. Ansari and S. S. Malhotra, Structure-activity relationship of some prepared Schiff bases as corrosion inhibitors for carbon steel in hydrochloric acid: Experimental and DFT insights, *Mater. Today Commun.*, 2025, **49**, 113843, DOI: 10.1016/j.mtcomm.2025.113843.

7 Q. A. Yousif, M. A. Bedair, A. M. Abuelela, A. Ansari, S. S. Malhotra and Z. Fadel, High-performance corrosion inhibitors for carbon steel in hydrochloric acid: electrochemical and DFT studies, *RSC Adv.*, 2025, **15**, 28666–28688, DOI: 10.1039/D5RA04952K.

8 Q. A. Yousif, M. A. Bedair, A. M. Abuelela, F. Al-odail, A. Ansari and Z. Fadel, Theoretical and experimental aspects of novel penicillanic acid compounds as corrosion inhibitors in acidic solutions, *Mater. Today Commun.*, 2025, **47**, 113199, DOI: 10.1016/j.mtcomm.2025.113199.

9 M. A. Bedair, A novel coumarin-azo Schiff base for dual corrosion inhibition for steel in acidic environments and anti-SRB protection: Experimental and computational insights, *Res. Surf. Interf.*, 2025, **19**, 100511, DOI: 10.1016/j.rsurfi.2025.100511.

10 N. Hossain, M. Asaduzzaman Chowdhury and M. Kchaou, An overview of green corrosion inhibitors for sustainable and environment friendly industrial development, *J. Adhes. Sci. Technol.*, 2021, **35**, 673–690, DOI: 10.1080/01694243.2020.1816793.

11 Y. K. Gautam, K. Sharma, S. Tyagi, A. Kumar and B. P. Singh, Chapter 6 – Applications of green nanomaterials in coatings, in *Green Nanomaterials for Industrial Applications*, ed, U. Shanker, C. M. Hussain and M. Rani , Elsevier, 2022, pp. 107–152, DOI: 10.1016/B978-0-12-823296-5.00014-9.

12 S. Yadav, A. P. S. Raman, M. B. Singh, I. Massey, P. Singh, C. Verma and A. AlFantazi, Green nanoparticles for advanced corrosion protection: Current perspectives and future prospects, *Appl. Surf. Sci. Adv.*, 2024, **21**, 100605, DOI: 10.1016/j.apsadv.2024.100605.

13 M. Pais and P. Rao, Green nanoparticles as a sustainable inhibitor to attenuate acid corrosion of zinc, *J. Mol. Struct.*, 2023, **1286**, 135634, DOI: 10.1016/j.molstruc.2023.135634.

14 P. E. Alvarez, M. V. Fiori-Bimbi, A. Neske, S. A. Brandán and C. A. Gervasi, Rollinia occidentalis extract as green corrosion inhibitor for carbon steel in HCl solution, *J. Ind. Eng. Chem.*, 2018, **58**, 92–99, DOI: 10.1016/j.jiec.2017.09.012.

15 H. Kumar, P. Yadav, R. Kumari, R. Sharma, S. Sharma, D. Singh, H. Dahiya, P. Kumar, S. Bhardwaj and P. Kaur, Highly efficient green corrosion inhibitor for mild steel in sulfuric acid: Experimental and DFT approach, *Colloids Surf., A*, 2023, **675**, 132039, DOI: 10.1016/j.colsurfa.2023.132039.

16 R. K. Mehta, S. K. Gupta and M. Yadav, Studies on pyrimidine derivative as green corrosion inhibitor in acidic environment: Electrochemical and computational approach, *J. Environ. Chem. Eng.*, 2022, **10**, 108499, DOI: 10.1016/j.jece.2022.108499.

17 Q. A. Yousif, M. A. Bedair, Z. Fadel, F. Al-Odail and A. M. Abuelela, Evaluating the efficacy of newly synthesized amino acid derivatives as corrosion inhibitors in acidic solutions, *Inorg. Chem. Commun.*, 2024, **164**, 112454, DOI: 10.1016/j.inoche.2024.112454.

18 A. M. Abuelela, J. Kaur, A. Saxena, M. A. Bedair, D. K. Verma and E. Berdimurodov, Electrochemical and DFT studies of Terminalia bellerica fruit extract as an eco-friendly inhibitor for the corrosion of steel, *Sci. Rep.*, 2023, **13**, 19367, DOI: 10.1038/s41598-023-45283-0.

19 M. A. Bedair, A. M. Abuelela, S. Melhi, Q. A. Yousif, V. V Chaban and E. H. Alosaimi, Highly effective inhibition of steel corrosion in 1.0 M HCl solution using a novel non-ionic surfactant with coumarin moiety: Practical and computational studies, *Mater. Chem. Phys.*, 2024, **312**, 128644, DOI: 10.1016/j.matchemphys.2023.128644.

20 A. M. Abuelela, M. A. Bedair, E. S. Gad, Y. F. El-Aryan, W. A. A. Arafa, A. K. Mourad, H. Nady and S. Eid, Exploring the synthesis, characterization, and corrosion inhibition of new tris-thiosemicarbazone derivatives for acidic steel settings using computational and experimental studies, *Sci. Rep.*, 2024, **14**, 13310, DOI: 10.1038/s41598-024-64199-x.

21 M. G. Gab-Allah, A. H. El-Ged, E. A. Badr, M. A. Bedair, S. A. Soliman and M. F. Bakr, Three novel Gemini amide amphiphilics synthesis, characterization, thermodynamics, surface properties and biological activity, *Egypt. J. Pet.*, 2023, **32**, 27–33, DOI: 10.1016/j.ejpe.2023.04.002.

22 M. Gab-Allah, M. A. Bedair, A. Elged, S. Soliman, E. Badr and M. Bakr, Empirical and Computational Investigation of Cationic Gemini Surfactants as Anti-Corrosive Inhibitors for Mild Steel in Acid Medium and its silver Nano Structure synthesis and Analysis, *Egypt. J. Chem.*, 2023, **66**(13), 2013–2031, DOI: 10.21608/ejchem.2023.222841.8256.

23 E. A. Badr, M. A. Bedair and S. M. Shaban, Adsorption and performance assessment of some imine derivatives as mild steel corrosion inhibitors in 1.0 M HCl solution by chemical, electrochemical and computational methods, *Mater. Chem. Phys.*, 2018, **219**, 444–460, DOI: 10.1016/j.matchemphys.2018.08.041.

24 S. A. A. Soliman, M. S. S. Metwally, S. R. R. Selim, M. A. A. Bedair and M. A. Abbas, Corrosion inhibition and adsorption behavior of new Schiff base surfactant on steel in acidic environment: Experimental and theoretical studies, *J. Ind. Eng. Chem.*, 2014, **20**, 4311–4320, DOI: 10.1016/j.jiec.2014.01.038.

25 M. J. Frisch, G. W. Trucks, H. B. Schlegel, G. E. Scuseria, M. A. Robb, J. R. Cheeseman, G. Scalmani, V. Barone, G. A. Petersson, H. Nakatsuji, X. Li, M. Caricato, A. V. Marenich, J. Bloino, B. G. Janesko, R. Gomperts, B. Mennucci, H. P. Hratchian, J. V. Ortiz, A. F. Izmaylov, J. L. Sonnenberg, D. Williams-Young, F. Ding, F. Lipparini, F. Egidi, J. Goings, B. Peng, A. Petrone, T. Henderson, D. Ranasinghe, V. G. Zakrzewski, J. Gao, N. Rega, G. Zheng, W. Liang, M. Hada, M. Ehara, K. Toyota, R. Fukuda, J. Hasegawa, M. Ishida, T. Nakajima, Y. Honda, O. Kitao, H. Nakai, T. Vreven, K. Throssell, J. A. Montgomery Jr, J. E. Peralta, F. Ogliaro, M. J. Bearpark, J. J. Heyd, E. N. Brothers, K. N. Kudin, V. N. Staroverov, T. A. Keith, R. Kobayashi, J. Normand,

K. Raghavachari, A. P. Rendell, J. C. Burant, S. S. Iyengar, J. Tomasi, M. Cossi, J. M. Millam, M. Klene, C. Adamo, R. Cammi, J. W. Ochterski, R. L. Martin, K. Morokuma, O. Farkas, J. B. Foresman and D. J. Fox, *Gaussian 16 Rev. C.01*, 2016.

26 R. Dennington, T. A. Keith, J. M. Millam, *GaussView Version 6*, 2019.

27 C. Lee, W. Yang and R. G. Parr, Development of the Colle-Salvetti correlation-energy formula into a functional of the electron density, *Phys. Rev. B: Condens. Matter Mater. Phys.*, 1988, **37**, 785–789, DOI: **10.1103/PhysRevB.37.785**.

28 A. D. Becke, Density-functional exchange-energy approximation with correct asymptotic behavior, *Phys. Rev. A*, 1988, **38**, 3098–3100, DOI: **10.1103/PhysRevA.38.3098**.

29 M. A. Bedair, E. H. Alosaimi and S. Melhi, A study of the inhibitive effect for corrosion of steel in 1.0 M HCl using a new nonionic surfactant based on coumarin moiety: chemical, electrochemical and quantum mechanics calculations, *J. Adhes. Sci. Technol.*, 2021, **37**, 1–31, DOI: **10.1080/01694243.2021.2018864**.

30 C. Jiang, G.-F. Wei, R. Lei, S. Deng, X. Li and D. Shao, Functional development of extracts from the invasive plant water hyacinth for steel corrosion protection, *npj Mater. Degrad.*, 2025, **9**, 33, DOI: **10.1038/s41529-025-00579-6**.

31 Y. Qiang, S. Zhang, B. Tan and S. Chen, Evaluation of Ginkgo leaf extract as an eco-friendly corrosion inhibitor of X70 steel in HCl solution, *Corros. Sci.*, 2018, **133**, 6–16, DOI: **10.1016/j.corsci.2018.01.008**.

32 R. Salim, E. Ech-chihbi, F. Benhiba, M. Ouakki, F. El Kalai, N. Benchat, W. Ettahiri, A. S. Alanazi, H. Oudda, B. Hammouti and M. Taleb, Corrosion inhibition and adsorption mechanism of novel imidazopyridine corrosion inhibitors: Electrochemical and computational studies, *J. Ind. Eng. Chem.*, 2025, **151**, 618–638, DOI: **10.1016/j.jiec.2025.04.033**.

33 L. H. Madkour, S. Kaya and I. B. Obot, Computational, Monte Carlo simulation and experimental studies of some arylazotriazoles (AATR) and their copper complexes in corrosion inhibition process, *J. Mol. Liq.*, 2018, **260**, 351–374, DOI: **10.1016/j.molliq.2018.01.055**.

34 Q. A. Yousif, S. S. Malhotra, M. A. Bedair, A. Ansari and A. K. Hadi, Safflower plant extract as a sustainable corrosion inhibitor for carbon steel in acidic media: a combined electrochemical and computational study, *RSC Adv.*, 2025, **15**, 21006–21025, DOI: **10.1039/D5RA03333K**.

35 L. Qiu, X. Li, B. Tan, Y. Xie and S. Deng, Agricultural waste of tobacco stem extract as a novel and efficient inhibitor for the corrosion of steel in HCl solution, *Ind. Crops Prod.*, 2025, **224**, 120367, DOI: **10.1016/j.indcrop.2024.120367**.

36 M. Kemel, Eco-friendly corrosion inhibition of steel using phenolic compounds from Cynara syriaca, *J. Ind. Eng. Chem.*, 2024, **140**, 617–630, DOI: **10.1016/j.jiec.2024.08.038**.

37 M. A. Bedair, H. M. Elaryian, E. S. Gad, M. Alshareef, A. H. Bedair, R. M. Aboushahba and A. S. Fouda, Insights into the adsorption and corrosion inhibition properties of newly synthesized diazinyl derivatives for mild steel in hydrochloric acid: synthesis, electrochemical, SRB biological resistivity and quantum chemical calculations, *RSC Adv.*, 2023, **13**, 478–498, DOI: **10.1039/D2RA06574F**.

38 B. Qiu, D. Zhang, T. Cheng, Y. Wang and H. Chu, Hydrodepolymerization of lignin for the preparation of phenolic monomers, aromatic hydrocarbons, and cycloalkanes: Factors evaluation, mechanism analysis, and challenges, *Chem. Eng. J.*, 2025, 166748, DOI: **10.1016/j.cej.2025.166748**.

39 N. Kedimar, P. Rao and S. A. Rao, Synthesis and characterization of pyridinium-based dicationic ionic liquid and its application in corrosion mitigation of 6061Al-10(vol%) SiC(p) composite in 0.05M HCl, *J. Mol. Liq.*, 2025, **435**, 128098, DOI: **10.1016/j.molliq.2025.128098**.

40 F. Luo, P. Yao, J. Zhang and E. Li, Alkyl pyridine ionic liquid as a green corrosion inhibitor for mild steel in acidic medium, *RSC Adv.*, 2025, **15**, 27369–27387, DOI: **10.1039/D5RA04148A**.

41 H. M. Elaryian, M. A. Bedair, A. H. Bedair, R. M. Aboushahba and A. E.-A. S. Fouda, Corrosion mitigation for steel in acid environment using novel p -phenylenediamine and benzidine coumarin derivatives: synthesis, electrochemical, computational and SRB biological resistivity, *RSC Adv.*, 2022, **12**, 29350–29374, DOI: **10.1039/D2RA05803K**.

42 M. A. A. Bedair, M. M. B. El-Sabbah, A. S. S. Fouda and H. M. M. Elaryian, Synthesis, electrochemical and quantum chemical studies of some prepared surfactants based on azodye and Schiff base as corrosion inhibitors for steel in acid medium, *Corros. Sci.*, 2017, **128**, 54–72, DOI: **10.1016/j.corsci.2017.09.016**.

43 M. A. A. Bedair, S. A. A. Soliman, M. F. Bakr, E. S. S. Gad, H. Lgaz, I.-M. M. Chung, M. Salama and F. Z. Alqahtany, Benzidine-based Schiff base compounds for employing as corrosion inhibitors for carbon steel in 1.0 M HCl aqueous media by chemical, electrochemical and computational methods, *J. Mol. Liq.*, 2020, **317**, 114015, DOI: **10.1016/j.molliq.2020.114015**.

44 B. Fan, H. Zhu, H. Li, H. Tian and B. Yang, Penetration of imidazoline derivatives through deposited scale for inhibiting the under-deposit corrosion of pipeline steel, *Corros. Sci.*, 2024, **235**, 112209, DOI: **10.1016/j.corsci.2024.112209**.

45 E. Berdimurodov, A. Kholikov, K. Akbarov and L. Guo, Inhibition properties of 4,5-dihydroxy-4,5-di-p-tolylimidazolidine-2-thione for use on carbon steel in an aggressive alkaline medium with chloride ions: Thermodynamic, electrochemical, surface and theoretical analyses, *J. Mol. Liq.*, 2021, **327**, 114813, DOI: **10.1016/j.molliq.2020.114813**.

46 M. A. Bedair, A. M. Abuelela, M. Alshareef, M. Owda and E. M. Eliwa, Ethyl ester/acyl hydrazide-based aromatic sulfonamides: facile synthesis, structural characterization, electrochemical measurements and theoretical studies as effective corrosion inhibitors for mild steel in 1.0 M HCl, *RSC Adv.*, 2023, **13**, 186–211, DOI: **10.1039/D2RA05939H**.

47 M. A. Bedair, In-depth assessment of new coumarin derivative based on azo dye and Schiff base as an effective corrosion inhibitor for steel in 1 M HCl solution and anti

sulphate reducing bacteria: Insights from computational and experimental techniques, *Inorg. Chem. Commun.*, 2024, **167**, 112693, DOI: 10.1016/j.inoche.2024.112693.

48 V. M. dos Santos, C. M. Fernandes, M. T. G. Sampaio, H. O. C. Junior, J. A. C. Velasco, B. F. Solano, A. Aldalbahi, L. X. Alvarez, H. Lgaz and E. A. Ponzio, DFT-guided design and experimental validation of small molecules to fight against mild steel corrosion: Chemical synthesis and extensive evaluation of 4 small enones as corrosion inhibitors, *Colloids Surf., A*, 2025, **726**, 137874, DOI: 10.1016/j.colsurfa.2025.137874.

49 W. Zhang, H.-J. Li, Y. Liu, D. Wang, L. Chen, L. Xie, L. Li, W. Zhang and Y.-C. Wu, Stevioside–Zn2+ system as an eco-friendly corrosion inhibitor for C1020 carbon steel in hydrochloric acid solution, *Colloids Surf., A*, 2021, **612**, 126010, DOI: 10.1016/j.colsurfa.2020.126010.

50 M. A. Abbas, E. I. Arafa, M. A. Bedair, A. S. Ismail, O. E. El-Azabawy, S. A. Baker and H. I. Al-Shafey, Synthesis, Characterization, Thermodynamic Analysis and Quantum Chemical Approach of Branched N, N′-bis(p-hydroxybenzoyl)-Based Propanediamine and Triethylenetetramine for Carbon Steel Corrosion Inhibition in Hydrochloric Acid Medium, *Arabian J. Sci. Eng.*, 2023, **48**, 7463–7484, DOI: 10.1007/s13369-022-07520-y.

51 S. Öztürk, Z. Gültekin, G. Akgül, G. Gece and L. O. Olasunkanmi, Resistance of di-cationic surfactant containing pyridinium ions to metal oxidation in 1.0 M HCl medium, *Appl. Surf. Sci.*, 2025, **692**, 162741, DOI: 10.1016/j.apsusc.2025.162741.

52 C. Che, M. Jiang, A. Li, K. Kang, J. Zhang, D. Huang and G. Li, Effect of Ni content on the corrosion resistance of CoCr0.8FeTi0.4Nix high entropy alloys in 3.5 wt% NaCl solution, *J. Alloys Compd.*, 2025, **1016**, 178900, DOI: 10.1016/j.jallcom.2025.178900.

53 H. M. Elaryian, M. A. Bedair, A. H. Bedair, R. M. Aboushahba and A. E.-A. S. Fouda, Synthesis, characterization of novel coumarin dyes as corrosion inhibitors for mild steel in acidic environment: Experimental, theoretical, and biological studies, *J. Mol. Liq.*, 2022, **346**, 118310, DOI: 10.1016/j.molliq.2021.118310.

54 T. N. Moeketse, P. G. Baker and P. R. Makgwane, Uric acid signal transduction enhancement through the electrical wiring of urate oxidase with copper Schiff base complex and reduced graphene oxide, *Electrochim. Acta*, 2025, **520**, 145837, DOI: 10.1016/j.electacta.2025.145837.

55 K. Ramakrishnan, S. Karthikeyan and D. Rajagopal, 2-Methoxy-4-(4-(((6-nitrobenzothiazol-2-yl)amino)methyl)-1-phenyl-1H-pyrazol-3-yl) phenol as powerful anti-corrosion inhibitor substantiated by Langmuir adsorption studies, *Mater. Lett.*, 2022, **313**, 131823, DOI: 10.1016/j.matlet.2022.131823.

56 A. Ait Mansour, K. Subbiah, H. Lgaz, M. R. Al-Hadeethi, M. Messali, T. Park, L. Bazzi, H. Lee and R. Salghi, Investigating corrosion failure in N80 carbon Steel: Experimental and theoretical insights into isonicotinohydrazide derivatives as inhibitors in acidic conditions, *Inorg. Chem. Commun.*, 2024, **161**, 112007, DOI: 10.1016/j.inoche.2023.112007.

57 J. A. Ramírez-Cano, A. Espinoza-Vázquez, A. Miralrio, A. Carmona-Hernandez, R. Galván-Martínez, M. Castro and R. Orozco-Cruz, Electrochemical and theoretical evaluation of loratadine as corrosion inhibitor for X65 steel in 1M HCl aqueous solution, *Int. J. Electrochem. Sci.*, 2024, **19**, 100843, DOI: 10.1016/j.ijoes.2024.100843.

58 M. A. Bedair, S. A. Soliman and M. S. Metwally, Synthesis and characterization of some nonionic surfactants as corrosion inhibitors for steel in 1.0 M HCl (Experimental and computational study), *J. Ind. Eng. Chem.*, 2016, **41**, 10–22, DOI: 10.1016/j.jiec.2016.07.005.

59 A. Ramachandran, P. Anitha, S. Gnanavel and S. Angaiah, Development of 1-phenyl-3-(4-(pyridin-4-ylmethyl)phenyl) urea derivatives as robust corrosion inhibitors for mild steel in 1 M HCl environment: Insight from ,molecular, experimental, and microscopic-scale modelling approaches, *J. Environ. Chem. Eng.*, 2024, **12**, 111648, DOI: 10.1016/j.jece.2023.111648.

60 M. M. Abdelsalam, M. A. Bedair, A. M. Hassan, B. H. Heakal, A. Younis, Z. I. Elbialy, M. A. Badawy, H. E.-D. Fawzy and S. A. Fareed, Green synthesis, electrochemical, and DFT studies on the corrosion inhibition of steel by some novel triazole Schiff base derivatives in hydrochloric acid solution, *Arabian J. Chem.*, 2022, **15**, 103491, DOI: 10.1016/j.arabjc.2021.103491.

61 M. Cheng, Q. Lyu, B. Shan, X. Zhao, Z. Wang, S. Sun, C. Li and S. Hu, Inhibitor-self-gated stimuli-responsive anticorrosion system based on π-π stacking, *Chem. Eng. J.*, 2020, **400**, 125917, DOI: 10.1016/j.cej.2020.125917.

62 F. Wang, S. Zhang, B. Tan, Y. Shi, X. Wang, H. Du, R. Liu and X. Han, Three anionic surfactants for corrosion inhibition in cobalt CMP: Research on validity and mechanism, *Surf. Interfaces*, 2024, **47**, 104202, DOI: 10.1016/j.surfin.2024.104202.

63 M. Ragab and M. A. Bedair, The effect of permanent magnet stirring on the corrosion resistance of Sn-2.0Ag-0.5Cu-2Zn solder alloys in NaCl solution, *Mater. Chem. Phys.*, 2023, **302**, 127774, DOI: 10.1016/j.matchemphys.2023.127774.

64 W. Emori, R. E. Odey, P. C. Okonkwo, D. I. Njoku, Y. Yang, P. C. Okafor and C. Cheng, Unveiling the potency of tetrahydropalmitine as a green anticorrosion material for 2024 aluminum alloy in acid-chloride environments, *J. Environ. Chem. Eng.*, 2024, **12**, 113809, DOI: 10.1016/j.jece.2024.113809.

65 S. Rmeid, A. Aridi, K. Habanjar, S. G. Elsharkawy and R. Awad, Identification of the structural characteristics, optical properties, and adsorption performance of Bi and Sn co-doped Co0.5Zn0.5Fe2O4 nanoparticles, *S. Afr. J. Chem. Eng.*, 2025, **53**, 267–280, DOI: 10.1016/j.sajce.2025.05.011.

66 M. Mobin, K. Cial, R. Aslam, S. Zamindar and P. Banerjee, Mitigation effect of a biodegradable surfactant N,N,N-trimethyl-2-(((hexadecyloxy)carbonyl)oxy)ethan-1-aminiumiodide for mild steel corrosion in 5% HCl: Experimental and theoretical insights, *Mater. Today*

Commun., 2024, **41**, 110696, DOI: 10.1016/j.mtcomm.2024.110696.

67 S. Melhi, M. A. Bedair, E. H. Alosaimi, A. A. O. Younes, W. H. El-Shwiniy and A. M. Abuelela, Effective corrosion inhibition of mild steel in hydrochloric acid by newly synthesized Schiff base nano Co(ii) and Cr(iii) complexes: spectral, thermal, electrochemical and DFT (FMO, NBO) studies, *RSC Adv.*, 2022, **12**, 32488–32507, DOI: 10.1039/D2RA06571A.

68 K. Dahmani, A. E. M. Ala Allah, Z. Aribou, O. Kharbouch, M. Galai, R. Almeer, M. E. Touhami, Y. Ramli, M. Cherkaoui, A. Chaouiki and Y. G. Ko, Imidazole derivative for corrosion protection: A comprehensive theoretical and experimental study on mild steel in acidic environments, *Colloids Surf., A*, 2025, **704**, 135376, DOI: 10.1016/j.colsurfa.2024.135376.

69 A. M. Abuelela, M. A. Bedair, E. S. Gad, Y. F. El-Aryan, W. A. A. Arafa, A. K. Mourad, H. Nady and S. Eid, Exploring the synthesis, characterization, and corrosion inhibition of new tris-thiosemicarbazone derivatives for acidic steel settings using computational and experimental studies, *Sci. Rep.*, 2024, **14**, 13310, DOI: 10.1038/s41598-024-64199-x.

70 M. Bedair, M. Metwally, S. Soliman, A. Al-Sabagh, A. Salem and T. Mohamed, Extracts Of Mint And Tea As Green Corrosion Inhibitors For Mild Steel In Hydrochloric Acid Solution, *Al-Azhar Bull. Sci.*, 2015, **26**, 1–14, DOI: 10.21608/absb.2015.23766.

71 A. Döner, R. Yıldız, S. Arslanhan and M. F. Baran, A comprehensive analysis of Arum dioscoridis plant leaf extract as a corrosion inhibitor for mild steel in 1 M HCl: Synthesis, characterization, surface analysis observations, experimental and DFT studies, *J. Taiwan Inst. Chem. Eng.*, 2025, **169**, 105955, DOI: 10.1016/j.jtice.2025.105955.

72 M. A. Bedair, H. M. Elaryian, A. H. Bedair, R. M. Aboushahba, A. El-Aziz and S. Fouda, Novel coumarin-buta-1,3-diene conjugated donor–acceptor systems as corrosion inhibitors for mild steel in 1.0 M HCl: Synthesis, electrochemical, computational and SRB biological resistivity, *Inorg. Chem. Commun.*, 2023, **148**, 110304, DOI: 10.1016/j.inoche.2022.110304.

73 K. W. Qadir, M. Doust Mohammadi and H. Y. Abdullah, Adsorption mechanism of CO, CO2, NO, NO2, and SO2 gases onto AlNNT(m,n)_k, (m = 5, 7; n = 0, 5, 7; k = 3–9), *Mater. Sci. Semicond. Process.*, 2025, **185**, 108973, DOI: 10.1016/j.mssp.2024.108973.

74 Y. H. Azeez, R. O. Kareem, R. A. Omer, L. O. Ahmed, I. N. Qader and K. A. Babakr, DFT and Monte Carlo Study of Chalcone Compounds as Corrosion Inhibitors: Influence of Various Substituents (R = Cl, Br, CH3, OCH3, NH2, OH, N(CH3)2, H, COOH), *Comput. Theor. Chem.*, 2025, **1247**, 115161, DOI: 10.1016/j.comptc.2025.115161.

75 Q. A. Yousif, Z. Fadel, A. M. Abuelela, E. H. Alosaimi, S. Melhi and M. A. Bedair, Insight into the corrosion mitigation performance of three novel benzimidazole derivatives of amino acids for carbon steel (X56) in 1 M HCl solution, *RSC Adv.*, 2023, **13**, 13094–13119, DOI: 10.1039/D3RA01837G.

76 M. A. Abbas and M. A. Bedair, Adsorption and Computational Studies for Evaluating the Behavior of Silicon Based Compounds as Novel Corrosion Inhibitors of Carbon Steel Surfaces in Acidic Media, *Z. Phys. Chem.*, 2019, **233**, 225–254, DOI: 10.1515/zpch-2018-1159.

77 S. S. Alarfaji, I. H. Ali, M. Z. Bani-Fwaz and M. A. Bedair, Synthesis and Assessment of Two Malonyl Dihydrazide Derivatives as Corrosion Inhibitors for Carbon Steel in Acidic Media: Experimental and Theoretical Studies, *Molecules*, 2021, **26**, 3183, DOI: 10.3390/molecules26113183.

78 H. Elmrayej, G. En-Nabety, R. Sghyar, K. I. Alaoui, H. Zejli, T. Benhadda, R. Haldhar, S.-C. Kim and M. Taleb, Dual-Functional N-Alkylated Tetrazole Derivatives: Corrosion Inhibitors with Potential for Pharmacological Development, *J. Mol. Struct.*, 2025, 144025, DOI: 10.1016/j.molstruc.2025.144025.